**Geomechanics and Engineering,** *Vol. 46, No. 1 (2026) 1-26*
https://doi.org/10.12989/gae.2026.46.1.000

Techno-Press

# Stability analysis of a circular tunnel constructed in soil with a circular void

Tao Liu[1], Rui Zhang*[1], Yao Xiao[2], Shilin Luo[1], Tiebiao Liu[3]

*[1]College of Civil Engineering, Changsha University, 98 Hongshan road, Kaifu district, Changsha, 410022, PR China*
*[2]College of Civil Engineering and Architecture, Guangxi University, 100 Daxue east road, Xixiangtang district, Guangxi, 530004, PR China*
*[3]Geophysical and Geochemical Survey Institute of Hunan Province, 898 Duan 2, Wanjiali south road, Tianxi district, Changsha, 410114, PR China*

*(Received March 15, 2026, Revised May 5, 2026, Accepted June 5, 2026)*

**Abstract.** This paper presents a comprehensive investigation into the stability of a circular tunnel constructed in soil containing a circular void. To achieve this, an adaptive finite element limit analysis (FELA) approach, combined with nonlinear programming (NLP), is employed. To enhance the convergence speed of the NLP algorithm, a novel approach is introduced, incorporating the feasible arc interior point algorithm (FAIPA) to perturb the search direction through a secondary deflection, and an imprecise step search algorithm to improve the efficiency of step length search. Based on the FELA method, both the upper bound (UB) and lower bound (LB) of the non-dimensional stability number are computed. Extensive parametric studies are conducted to evaluate the effects of key parameters on tunnel stability. The computational results are effectively conveyed through the utilization of dimensionless stability tables and charts, specifically designed to facilitate ease of use by engineers. Furthermore, meticulous examination of typical failure mechanisms provides deep insights into the complex behavior of tunnels under varying conditions.

**Keywords:** finite element limit analysis; imprecise step search; nonlinear programming; stability; tunnels

## 1. Introduction

The accurate assessment of tunnel stability is a critical task in ensuring safe design and construction practices in the field of tunnelling. Several studies have been conducted to determine the stability of single tunnels, using analytical methods [1],[2], [3], [4] and numerical simulations [5], [6-7], [8], [9], [10], [11], [12], [13], [14]. In practical engineering, encountering strata containing voids during tunnel construction is a common yet hazardous scenario. The existence of voids can be categorized into two distinct types: natural formations due to chemical activities, such as the dissolution of soluble substances (e.g., karst caves), and artificial cavities resulting from human activities like mining, tunnelling, and drilling. The presence of these adjacent underground voids significantly disrupts the continuity of the soil mass, inherently altering the primary stress field and creating localized zones of stress concentration. When a new tunnel is excavated in such

*Corresponding author, Assistant Professor, E-mail: z20190809@ccsu.edu.cn


http://www.techno-press.org/gae/5
ISSN: 2005-307X (Print), 2092-6219 (Online)

disturbed strata, the complex stress redistribution often leads to asymmetric earth pressures acting on the tunnel lining, exacerbated ground surface settlements, and a higher susceptibility to localized shear failures. If not rigorously evaluated, this tunnel-void interaction can trigger severe construction hazards, including excessive deformation, face instability, or even catastrophic ground collapse. As a result, a comprehensive assessment of tunnel stability in the presence of adjacent voids is imperative for ensuring safe design and construction practices.

In contrast to a solitary tunnel, the stability and failure mechanisms of tunnels influenced by neighboring voids are notably governed by the center-to-center distance. In view of these issues, numerous research endeavors have been undertaken to scrutinize the stability of dual tunnels in soft soils using various methods, including finite element limit analysis (FELA) [15], [16-17], [18-19], [20], small-scale model tests [21], centrifuge model tests [22], [23], [24-26], upper bound solutions [27], and UB FELA methods [28-29], [30], [31-32]. These studies have examined various aspects of dual tunnels, including the effects of closely spaced tunnels, arching effects, and required lining pressure. Furthermore, stability analyses have also been conducted for dual tunnels in rock masses subjected to surcharge loading, using the generalized Hoek-Brown criterion [33], [34], [35], [36].

Previous studies, as mentioned above, have primarily focused on the stability of twin tunnels with the same depths and diameters. However, considering the potential variability in void formation around tunnels due to various factors, such as different causes of void formation, the size and burial depth of voids may vary from those of the constructed tunnels. Although some studies have investigated the stability of tunnels with different burial depths (e.g., Chehade and Shahrour [37], Banerjee and Chakraborty [38], Xiao et al. [39], and La and Kim [40]), the influence of void size around the tunnels has not been addressed.

This paper investigates the stability problems of a circular tunnel constructed in soil with a circular void by using the FELA method in conjunction with NLP technique. Notably, the approach employed in this study builds upon the methods used in our previous research [34], [39], [11], [33] and introduces two key innovations. Firstly, a novel inexact step search technique is proposed to enhance the efficiency of step length search in the NLP algorithm's step search phase. Secondly, in the Newton iteration process, the challenge of finding an initial feasible point is circumvented by incorporating the residual term corresponding to the unbalanced force into the right-hand side of the linear equations. These enhancements significantly improve the convergence speed of the NLP algorithm [41-42]. Based on the FELA method, rigorous upper and lower bounds of the dimensionless tunnel stability number are obtained, and the calculated results are summarized in design tables and charts that can be readily utilized by practitioners. Furthermore, the effects of relative positions and soil properties on the tunnel stability number are thoroughly discussed, along with an in-depth analysis of the failure mechanics. To validate the proposed method, the results are compared with solutions reported in the existing literature for verification purposes.

## 2. Problem definition

Fig. 1 illustrates the proposed model, which takes into consideration the main geometric parameters, under plane strain conditions. The model consists of a circular tunnel A with a diameter $D$, constructed in soil that contains a circular void B with a diameter $R$. Tunnel A is located at a depth $H$ below the ground surface, without any surcharge loading. The symbols $S$ and

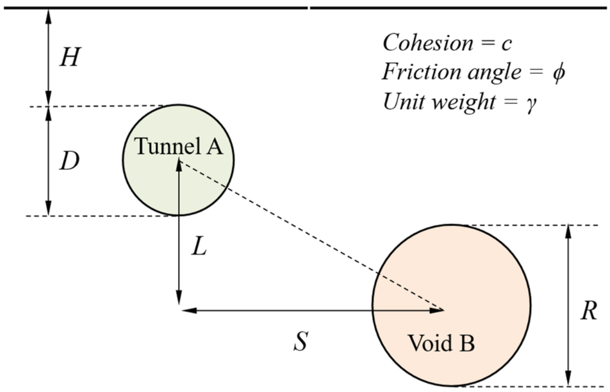


Figure 1. Definition of the problem

$L$ denote the horizontal and vertical distances between the centers of the tunnel and the void, respectively. The soil surrounding the tunnels is assumed to be homogeneous and isotropic, with cohesion $c$, frictional angle $\phi$, and unit weight $\gamma$. The soil follows the Mohr-Coulomb yield criterion and an associated flow rule.

To present the results in a concise manner, the critical soil weight $\gamma_{cr}$ is expressed in terms of the dimensionless stability number $N$, which is a function of $\phi$, $H/D$, $S/D$, $R/D$ and $L/D$, as given by the Eq. (1).

$$N = \frac{\gamma_{\mathrm{cr}} D}{c} = f\left(\phi, \frac{H}{D}, \frac{S}{D}, \frac{R}{D}, \frac{L}{D}\right) \tag{1}$$

To construct a series of stability tables and charts for design purposes, in this study, the ranges of the problem parameters are for $\phi$ = 5°-20°, $H/D$ = 1-5, $S/D$ = 1.5-12, $R/D$ = 0.5-1.5 and $L/D$ = 0-2.

## 3. Method of analysis

The FELA computational method combines classical plasticity limit theorems with finite elements and modern convex optimization, making it a highly attractive option for conducting geotechnical stability analyses [43]. Given its high efficiency, the FELA method is employed in this work to investigate the problem at hand. In the ensuing sections, this paper elucidates on several key implementation details associated with the FELA method.

### 3.1 Discretization of finite elements

In this study, we employed linear-stress and linear-velocity triangular elements to discretize the problem framework in the LB and UB analyses, respectively. The linear-stress triangular element, as depicted in Fig. 2(a), is characterized by the horizontal normal stress $\sigma_{xx}$, vertical normal stress $\sigma_{yy}$, and shear stress $\tau_{xy}$ as basic variables at each node. Additionally, each element is subject to two unknown body forces $h_x^e$ and $h_y^e$. On the other hand, the linear-velocity triangular element, as illustrated in Fig. 2(b), is characterized by the primary variables of horizontal velocity $u_x$ and

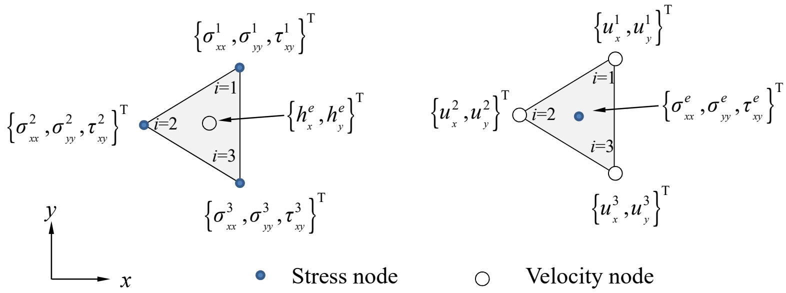


(a) Lower bound element (b) Upper bound element

Figure 2. Lower bound and upper bound elements

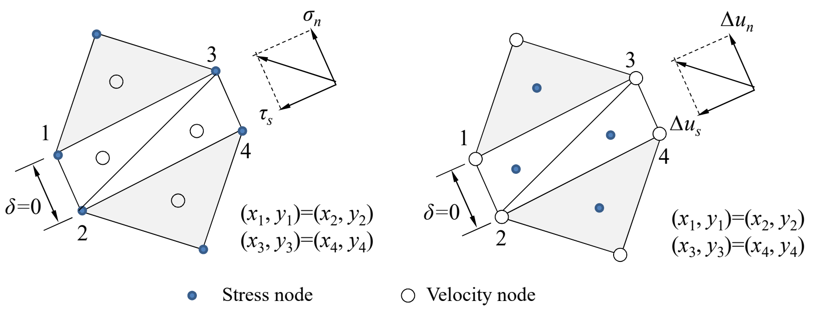


(a) Statically admissible stress discontinuity (b) Kinematically admissible velocity discontinuity

Figure 3. Stress and velocity discontinuities

vertical velocity $u_y$ at each node. Furthermore, each element is subject to three unknown stresses, $\sigma^e_{xx}$, $\sigma^e_{yy}$, and$\tau^e_{xy}$. However, the modelling of complex stress or velocity fields is limited by the use of lower-order linear elements. To address this issue and improve the accuracy of the failure load analysis, Lyamin et al. [44] proposed incorporating stress discontinuities, while Krabbenhoft et al. [45] suggested using velocity discontinuities. In this regard, the LB and UB solutions implement the stress and velocity discontinuities, respectively, along all inter-element edges. The discontinuities are represented as two triangles of zero thickness, forming a continuum element. Fig. 3 illustrates the opposing nodal pairs having the same coordinates. This approach improves the modelling of stress and velocity fields, thereby enhancing the accuracy of the failure load analysis.

### 3.2 Establishment of optimization models

By employing the method of discretization of the static form of limit analysis with the application of the discontinuous finite element interpolation space, along with the integration of equations and inequality constraints associated with both continuous and discontinuous elements, two optimization models of identical form can be derived as follows

$$\text{Maximize} \quad \alpha \tag{2}$$

$$\text{Subject to} \quad \mathbf{B}^{\mathrm{T}}\boldsymbol{\sigma} = \alpha\mathbf{p} + \mathbf{p}_0 \tag{3}$$

$$f(\boldsymbol{\sigma}_j) \leq 0, j = 1, \dots N \tag{4}$$

where $\alpha$ is a load multiplier, $\mathbf{B}^{\mathrm{T}}$ is the discrete equilibrium-type operator, $\boldsymbol{\sigma} = (\boldsymbol{\sigma}_1, \dots, \boldsymbol{\sigma}_N)^{\mathrm{T}}$ is the vector of discrete stresses $\boldsymbol{\sigma}_j$, and $N$ is the total number of discrete stresses; $\mathbf{p}$ and $\mathbf{p}_0$ are the vectors of unknown and prescribed nodal forces, respectively, and $f$ is the yield function.

It is noteworthy that the static form of limit analysis allows for the elimination of the velocity variable $\mathbf{u}$ from the initial optimization model. Consequently, the optimization model expressed by Eqs. (2)-(4) only involves the stress variable $\boldsymbol{\sigma}$, with no direct involvement of $\mathbf{u}$. A typical approach for solving such optimization models is by using a primal-dual algorithm. This algorithm is notable for its ability to solve both the primal and dual problems of the UB and LB optimization models concurrently. As such, the dual problems represented by Eqs. (5)-(8) account for the velocity variable $\mathbf{u}$ and its associated constraints.

$$\textbf{Minimize} \quad \boldsymbol{\sigma}^{\mathrm{T}}(\nabla\mathbf{f} \cdot \boldsymbol{\lambda}) - \mathbf{p}_0^{\mathrm{T}}\mathbf{u} \tag{5}$$

$$\textbf{Subject to} \quad \mathbf{Bu} - \nabla\mathbf{f} \cdot \boldsymbol{\lambda} = 0 \tag{6}$$

$$\mathbf{p}^{\mathrm{T}}\mathbf{u} = 1 \tag{7}$$

$$\boldsymbol{\lambda} \geq \mathbf{0} \tag{8}$$

where $\mathbf{u}$ is the vector of velocities, $\boldsymbol{\lambda}$ is the vector of plastic multipliers and $\mathbf{f}$ represents all plastic yielding functions composed of vector-valued functions.

Note that if the complementary condition $\boldsymbol{\lambda} \cdot \mathbf{f}(\boldsymbol{\sigma}) = \mathbf{0}$ is satisfied, the duality gap between the primal and dual problems is equal to zero (i.e., $\boldsymbol{\sigma}^{\mathrm{T}}(\nabla\mathbf{f} \cdot \boldsymbol{\lambda}) - \mathbf{p}_0^{\mathrm{T}}\mathbf{u} - \alpha = 0$). This means that the primal and dual problems are exactly equivalent.

### 3.3 Calculation method for the optimization models

Following the convex optimization theory [46], the discrete optimization models represented by Eqs. (2)-(8) can be solved if the optimization variables ($\boldsymbol{\sigma}$, $\mathbf{u}$, $\boldsymbol{\lambda}$) satisfy the following Kuhn-Tucker optimization conditions

$$\mathbf{B}^{\mathrm{T}}\boldsymbol{\sigma} = \alpha\mathbf{p} + \mathbf{p}_0 \tag{9}$$

$$\mathbf{Bu} = \nabla\mathbf{f} \cdot \boldsymbol{\lambda} \tag{10}$$

$$\mathbf{p}^{\mathrm{T}}\mathbf{u} = 1 \tag{11}$$

$$\mathbf{f} \cdot \boldsymbol{\lambda} = 0 \tag{12}$$

$$\mathbf{f}(\boldsymbol{\sigma}) \leq 0 \tag{13}$$

$$\boldsymbol{\lambda} \geq 0 \tag{14}$$

The primal-dual interior-point algorithm is a nonlinear algorithm that is capable of efficiently solving the Kuhn-Tucker optimization conditions mentioned above. To ensure the effectiveness of the algorithm, the search direction of each iteration must be feasible. However, in the presence of highly nonlinear inequality constraints, the linear search step length may become excessively small, significantly reducing the convergence speed of the NLP algorithm. To address this issue, researchers have proposed different NLP algorithms using the one-time deflection perturbation technique. For instance, Borges et al. [47], Lyamin and Sloan [48-49], and Krabbenhøft et al. [50-51] have developed various methods to suitably modify the linear search direction by considering the curvature of the feasible domain boundary. Despite their effectiveness, the small search step length obtained by using these methods near the sharp point of the yield surface can affect the overall convergence speed of the NLP algorithm. To mitigate this problem, this paper introduces the feasible arc interior point algorithm (FAIPA) proposed by Herskovits et al. [52] that achieves a quadratic deflection perturbation of the linear search direction. The solution steps of this method are summarized as follows:

First, the Newton method is used to linearize the Kuhn-Tucker optimization conditions represented by Eqs. (9)-(14). The resulting linear system of equations is then solved to obtain the initial incremental estimate $\mathbf{d}^0$. Second, two perturbations are introduced to the right-hand side of the original linear equations. This enables the determination of both the feasible direction $\mathbf{d}$ and the recovery direction $\tilde{\mathbf{d}}$, which are obtained by solving the perturbed linear equations. Next, a feasible arc $\mathbf{x}(t)$ is constructed at the current iteration point $\bar{\mathbf{x}}$, which is described by Eq. (15), where $t$ represents the allowable step length. A linear search is then performed along the feasible arc to determine the value of $t$. Finally, the iteration points are updated, and the program checks if it satisfies the convergence requirement. If the requirement is satisfied, the program ends. If not, the process continues to the next iteration.

$$\mathbf{x}(t) = \bar{\mathbf{x}} + t\mathbf{d} + t^2\tilde{\mathbf{d}} \tag{15}$$

The schematic depiction of the feasible arc is shown in Fig. 4. It can be noted that the feasible arc is tangent to the recovery direction $\tilde{\mathbf{d}}$ as $t$ approaches infinity (i.e., $t = +\infty$), and is tangent to the feasible direction $\mathbf{d}$ at the current iteration point (i.e., $t = 0$). The allowable step length $t$ can be enlarged whilst traversing this arc as it possesses a curvature similar to the boundary of the feasible domain. Consequently, the NLP algorithm's convergence rate can be enhanced effectively.

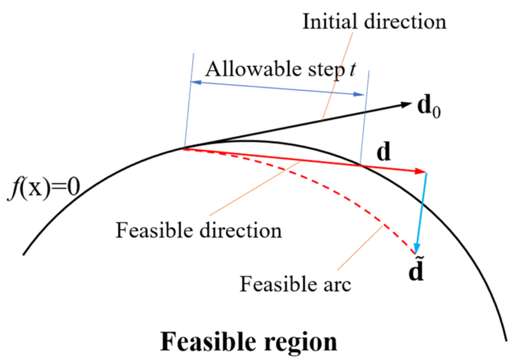


Figure 4. Illustration of the feasible arc

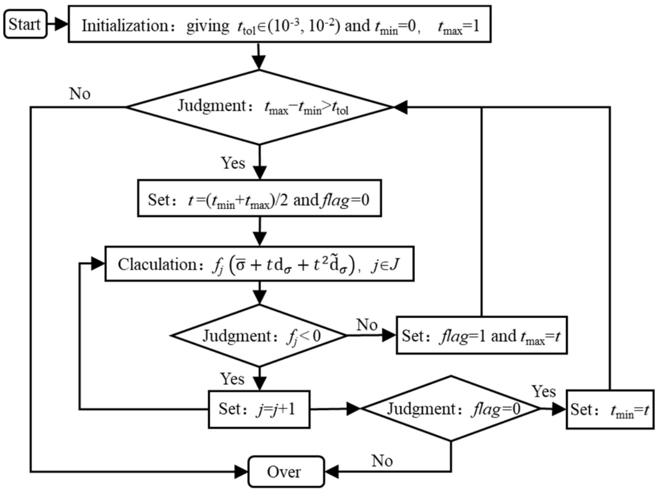


Figure 5. Flowchart of imprecise step length search algorithm

### 3.4 Determination of the iteration step length

After defining the feasible arc, it becomes essential to determine a reasonable iteration step length $t$ along the arc. In previous studies conducted by the authors [34], [39], [11], [33], the exact search technique proposed by Lyamin and Sloan [48-49] was utilized for calculating the permissible step length, which can be expressed as Eq. (16)

$$t = \min\left[\min_{j\in J_\sigma} t_j \,|\, f_j(\mathrm{x}+t_j\mathbf{d}_j) = \delta_f f_j(\mathrm{x}),1\right] \tag{16}$$

where the parameter $\delta_f$ will gradually converge to 0, which can be obtained by Eq. (17)

$$\delta_f = \min\left[\delta_0^f, \|\mathrm{c}^{\mathrm{T}}\mathbf{d}_0\| / \|\mathbf{c}^{\mathrm{T}}\mathbf{x}\|\right] \tag{17}$$

where $\delta_0^f \in (0,1)$.

The implementation of the exact search strategy at hand entails a sequential search for each inequality constraint, followed by a determination of the minimum search step as the final iteration step length. However, this approach requires a significant amount of computational time to be devoted to the step search stage, which in turn impairs the overall efficiency of the solution. In this work, a new imprecise step search algorithm is proposed by the authors, which can be summarized as follows:

**Step 1**: The allowable error, $t_{\mathrm{tol}} \in (10^{-3},\ 10^{-2})$, is given. The lower and upper limits of the step length $t$ are set to $t_{\mathrm{min}} = 0$ and $t_{\mathrm{max}} = 1$, respectively.

**Step 2**: If $t_{\mathrm{max}} - t_{\mathrm{min}} > t_{\mathrm{tol}}$, the step length is updated to $t = (t_{\mathrm{max}} + t_{\mathrm{min}})/2$, and the *flag* is set to 0. Otherwise, the current step length $t$ is considered the result, and the program terminates.

**Step 3**: Starting from $j$ = 1, for all $j \in J$, the value of $f_j(\bar{\boldsymbol{\sigma}} + t\boldsymbol{d}_\sigma + t^2\tilde{\boldsymbol{d}}_\sigma)$ is calculated, and the sign of $f_j$ is determined. If $f_j < 0$, $j$ is incremented by 1, and the next $f_j$ is evaluated. Otherwise, the *flag* is set to 1, $t_{\mathrm{max}}$ is updated to 1, and the program returns to step 2.

**Step 4**: If *flag* = 0, $t_{\min}$ is updated to $t$, and the program returns to step 2. Otherwise, no feasible step length is found, and the program terminates.

The step length search algorithm also can be illustrated using the flowchart presented in Fig. 5. The figure shows that the allowable step interval [$t_{\min}$, $t_{\max}$] is halved in each iteration of the outer loop (main loop). Typically, for a tolerance error of $t_{\text{tol}} \in (10^{-3},\ 10^{-2})$, the search requires only 7-10 iterations. The step length search algorithm possesses excellent numerical stability and solving efficiency. This can be attributed to the algorithm's ability to terminate the inner loop and skip the next iteration of the outer loop, once the current step length $t$ violates a certain inequality constraint $f_j$, thus improving the search efficiency. Additionally, if the current search direction is feasible, the step length lower limit $t_{\min}$ must be a feasible step length, ensuring program stability.

### 3.5 Initialization requirements

The approach adopted in this investigation accounts for the residual term resulting from the presence of unbalanced forces. As such, the initial iteration point $\mathbf{x}_0 = (\bar{\alpha}^0,\ \bar{\boldsymbol{\sigma}}^0)$ need not conform to the equilibrium equation but must only meet the stress yield condition. This premise allows for the establishment of the initial iteration point as Eq. (18)

$$\bar{\alpha}^0 = 0,\quad \bar{\boldsymbol{\sigma}}^0 = \mathbf{0} \tag{18}$$

On the one hand, the current NLP algorithm must ensure that $\bar{\boldsymbol{\lambda}}$ remains positive throughout the process, and it may be initialized to $\bar{\lambda}_j^0 = 1/f_j(\mathbf{0})$. It is noteworthy that the methodology proposed by Lyamin and Sloan [48-49] necessitates the resolution of an initial stage problem to obtain the initial feasible point. In contrast, the present approach has relaxed the equation constraints, thereby obviating the need to search for the initial feasible point. Consequently, the convergence speed of the NLP algorithm has been significantly enhanced.

### 3.6 Mesh adaptivity of FELA

Controlling the relative errors between the LB and UB is a crucial aspect of the FELA method. To this end, the employment of adaptive mesh refinement techniques has been proven to be an efficient approach for reducing the relative errors and achieving tight bounds on the limit load. This paper proposes the incorporation of an adaptive remeshing procedure, developed by the first author [53], into the aforementioned FELA program. The proposed procedure is designed to adjust the element sizes in the mesh, enabling the uniform distribution of local errors across all elements in the domain. The mesh-updating criterion presented by Zhang et al. [53] can be expressed as Eqs. (19)-(20)

$$d_{new}(\mathbf{x}) = \beta(\mathbf{x}) \cdot d_{old}(\mathbf{x}),\ \mathbf{x} \in \Omega \tag{19}$$

$$\text{s.t.}\quad \underline{\beta} \le \beta(\mathbf{x}) = \frac{\sqrt{4\Delta \Big/ \left(\sqrt{3} Nel \cdot \rho(\mathbf{x})\right)}}{d_{old}(\mathbf{x})} \le \overline{\beta} \tag{20}$$

where *Nel* is the total number of elements specified for the new mesh; $d_{old}$ and $d_{new}$ are the distributions of element sizes in the old and new meshes, respectively; $\beta(\mathbf{x})$ is the distribution of the decreasing or increasing rate of element sizes in the new mesh subject to the upper and lower

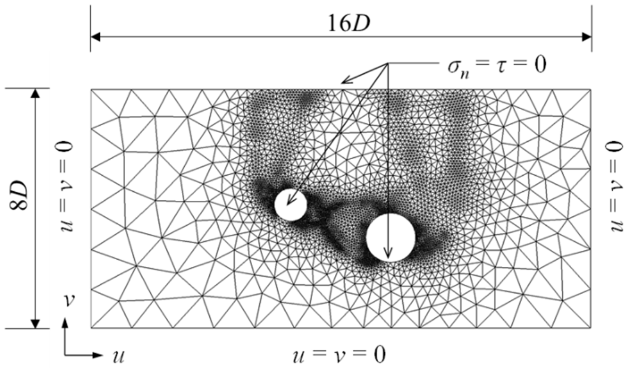


Figure 6. Adaptive mesh for the case of $R/D$=1.5, $H/D$=3 and $S/D$ =3 and the corresponding boundary conditions

limits of $\bar{\beta}$ and $\underline{\beta}$; $\rho(\mathbf{x})$ is the distribution of the intensity of dissipation gap; $\Delta$ is the overall dissipation gap.

The specificities pertaining to the adaptive remeshing procedure have been comprehensively described by Zhang et al. [53]. However, for the sake of simplicity, these particular details have been omitted herein.

## 4. Numerical simulations

The current study presents a typical adaptive mesh for the investigated problem with $R/D$=1.5, $H/D$=3 and $S/D$ =3, as illustrated in Fig. 6. The mesh comprises 7646 triangular elements and 13156 stress-velocity discontinuities, and similar meshes are employed for both the LB and UB analyses. The LB analyses are subject to normal and shear stresses ($\sigma_n$, $\tau$) as boundary conditions, while the UB analyses are prescribed with kinematic restraints on the horizontal and vertical velocities ($u$, $v$). To ensure the reliability of the numerical results, the problem domain size is chosen to be sufficiently large (i.e., a length of 16 times the tunnel diameter (16$D$) and a width of 8 times the tunnel diameter (8$D$)) to enclose all plastic yielding zones completely, and the boundary conditions do not interfere with the numerical calculations. The adaptive remeshing procedure is performed iteratively for three iterations to obtain tight bounds for the investigated problem. The initial iteration adopts a mesh with 1000 elements, and the number of elements increases to around 8000 in the third iteration. It is worth mentioning that the adaptive meshing iterations are adequately set to control the relative errors between the LB and UB, as measured by Eq. (21), within 4% or better. Therefore, the numerical simulations are deemed accurate and reliable.

It should be emphasized that this rigorous control of the relative error effectively demonstrates the robustness of the numerical results against mesh sensitivity. Because the exact stability number is mathematically bracketed by the LB and UB solutions, converging these bounds to within a narrow margin of 4% guarantees a high degree of accuracy. Consequently, any further mesh refinement would only produce negligible changes to the stability numbers, constrained strictly within this tight bounding envelope. This confirms that the numerical solutions have sufficiently converged, and the main trends observed in the subsequent parametric studies are entirely robust and free from artifacts related to mesh dependency.

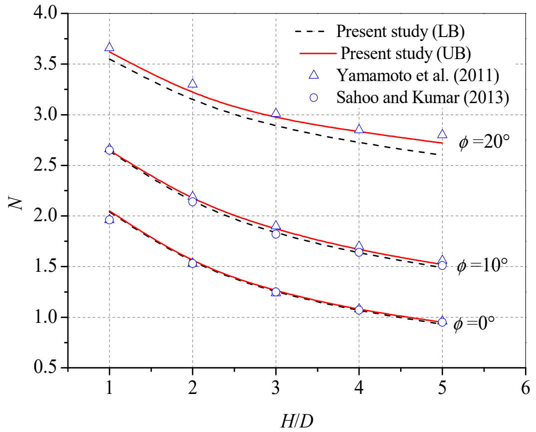


Figure 7. Comparison of variation in $N$ with $H/D$ for a single isolated circular tunnel ($R/D$=0, $S/D$=0 and $L/D$=0)

$$\text{Relative error} = 100 \times (\text{UB} - \text{LB}) / (\text{UB} + \text{LB})\ (\%) \tag{21}$$

In Eq. (21), the term ($UB$+$LB$) in the denominator represents twice the arithmetic mean of the upper and lower bounds. Since the exact stability number is unknown but strictly bracketed by the $LB$ and $UB$, their average value ($UB$+$LB$)/2 serves as the best estimate. Consequently, dividing the maximum absolute error ($UB$-$LB$)/2 by this average estimate mathematically yields the relative error ($UB$-$LB$)/($UB$+$LB$). This formulation is a standard and rigorous convention in limit analysis for symmetrically evaluating the error margin.

## 5. Results and discussions

### 5.1 Comparisons of stability numbers

For verification purposes, the stability numbers obtained from the current study for a single isolated circular tunnel are first compared with the results of the UB FELA method by Sahoo and Kumar [28], which is based on linear programming, and the FELA approach of Yamamoto et al. [9], which uses nonlinear programming. The results of Yamamoto et al. [9] are the average of the LB and UB solutions. Fig. 7 shows the variation of the stability number $N$ with $H/D$ for the cases of $R/D$=0, $S/D$=0 and $L/D$=0. It can be seen that the present solutions demonstrate good agreement with the results of Sahoo and Kumar [28] and Yamamoto et al. [9].

For dual circular tunnels with the same diameters and depths, a further comparison of the present study is made with (i) the UBFEM-RTME method of Zhang et al. [32] and (ii) the LB and UB FELA results of Yamamoto et al. [16]. Fig. 8 illustrates the variation of the stability number $N$ with $S/D$ for the cases of $R/D$=1, $H/D$=3 and $L/D$=0. As seen, the results of the present study and those of Zhang et al. [31] and Yamamoto et al. [16] are in excellent agreement. It also can be observed that, for the case of $\phi$ = 20°, the relative errors of the present analysis are lower than those of Yamamoto et al. [16], potentially due to the use of an adaptive remeshing approach in the current solutions.

Table 1. Comparison of results for different algorithms

| Soil Parameters | | Element type | Adaptive Step | Strategy 1 (Present study) | | | Strategy 2 (Lyamin and Sloan [48-49]) | | |
|---|---|---|---|---|---|---|---|---|---|
| *c* (kPa) | *ϕ* (°) | | | No. Iter. | Time (s) | *N* | No. Iter. | Time (s) | *N* |
| 10 | 5° | "Lower" | 1 | 23 | 0.455 | 1.192 | 25 | 0.495 | 1.196 |
| | | | 2 | 20 | 1.698 | 1.214 | 24 | 2.038 | 1.218 |
| | | | 3 | 18 | 2.995 | 1.220 | 21 | 3.494 | 1.223 |
| 10 | 5° | "Upper" | 1 | 15 | 0.285 | 1.407 | 19 | 0.361 | 1.409 |
| | | | 2 | 21 | 1.586 | 1.277 | 27 | 2.039 | 1.283 |
| | | | 3 | 22 | 3.408 | 1.250 | 33 | 5.112 | 1.249 |
| 10 | 20° | "Lower" | 1 | 26 | 0.592 | 2.308 | 31 | 0.706 | 2.318 |
| | | | 2 | 17 | 1.616 | 2.527 | 26 | 3.865 | 2.534 |
| | | | 3 | 20 | 3.802 | 2.582 | 24 | 4.562 | 2.578 |
| 10 | 20° | "Upper" | 1 | 17 | 0.340 | 3.623 | 18 | 0.362 | 3.612 |
| | | | 2 | 22 | 1.721 | 2.968 | 26 | 2.034 | 2.981 |
| | | | 3 | 21 | 3.846 | 2.777 | 29 | 5.311 | 2.774 |
| 10 | 30° | "Lower" | 1 | 20 | 0.442 | 3.621 | 28 | 0.619 | 3.628 |
| | | | 2 | 15 | 1.423 | 4.347 | 32 | 3.136 | 4.351 |
| | | | 3 | 23 | 4.051 | 4.637 | 43 | 7.574 | 4.643 |
| 10 | 30° | "Upper" | 1 | 41 | 0.806 | 9.806 | 59 | 1.159 | 9.827 |
| | | | 2 | 22 | 1.704 | 5.375 | 68 | 5.267 | 5.391 |
| | | | 3 | 58 | 7.482 | 5.022 | 94 | 12.146 | 5.036 |

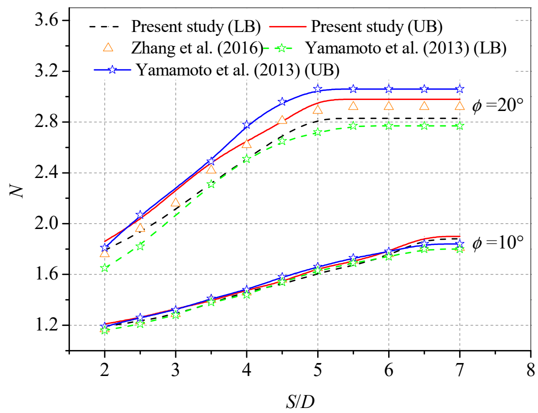


Figure 8. Comparison of variation in *N* with *S*/*D* for dual circular tunnels (*R*/*D*=1, *H*/*D*=3 and *L*/*D*=0)

To further evaluate the computational efficiency of the proposed NLP solution procedure, a quantitative comparison was conducted between the current strategy and the algorithm developed by Lyamin and Sloan [48-49]. This comparison was performed on a representative dual-tunnel case with geometric configurations of *R*/*D*=0.5, *H*/*D*=3, *S*/*D*=2 and *L*/*D*=1. The analysis employed an adaptive remesh process starting from an initial mesh of 1,000 elements and terminating at approximately 8,000 elements after three refinement iterations.

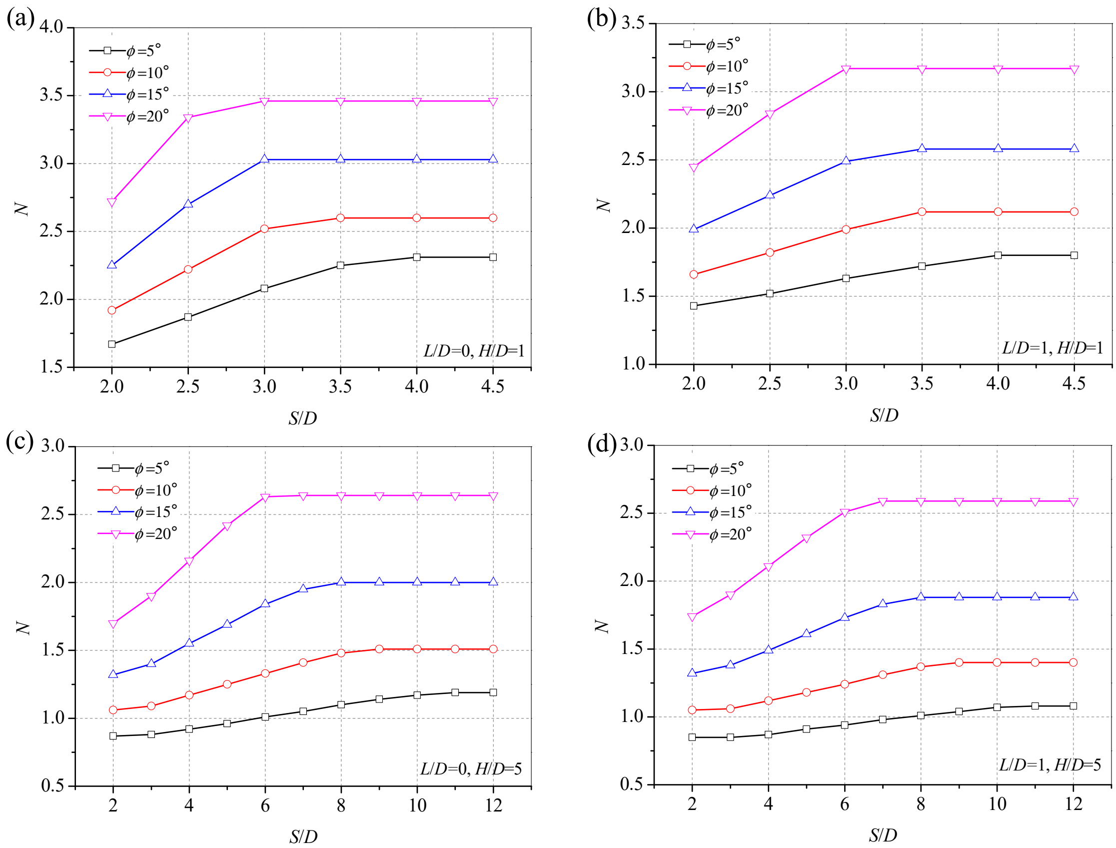


Figure 9. The variations of N with S/D and ϕ for the case of R/D=1: (a) L/D=0, H/D=1, (b) L/D=1, H/D=1, (c) L/D=0, H/D=5 and (d) L/D=1, H/D=5

Table 1 summarizes the iteration counts and computational time for both methods under various soil parameters (c and $\phi$) using both lower and upper bound elements. It can be observed that the proposed method consistently requires fewer iterations to reach convergence compared to the single-perturbation NLP approach used by Lyamin and Sloan [48-49]. Specifically, the reduction in iteration numbers leads to a marked decrease in the total CPU time.

## 5.2 Analyses of stability numbers

In this study, the upper and lower bounds of the stability number *N* for a circular tunnel constructed in soil with a circular void have been calculated. The relative errors between these estimates have been determined to be within 4% or better, indicating a high degree of accuracy in the obtained results. Consequently, the average values of the upper and lower bound stability number *N* have been utilized in subsequent discussions. The calculated results of the AFELA program, developed by the authors, have been summarized in Tables 2-4 and illustrated graphically in Figs. 9-12.

Generally, the results presented in Figs. 9-12 can be categorized into two distinct types. Firstly, the stability number increases continuously with an increasing value of *S*/*D*, up to a critical value

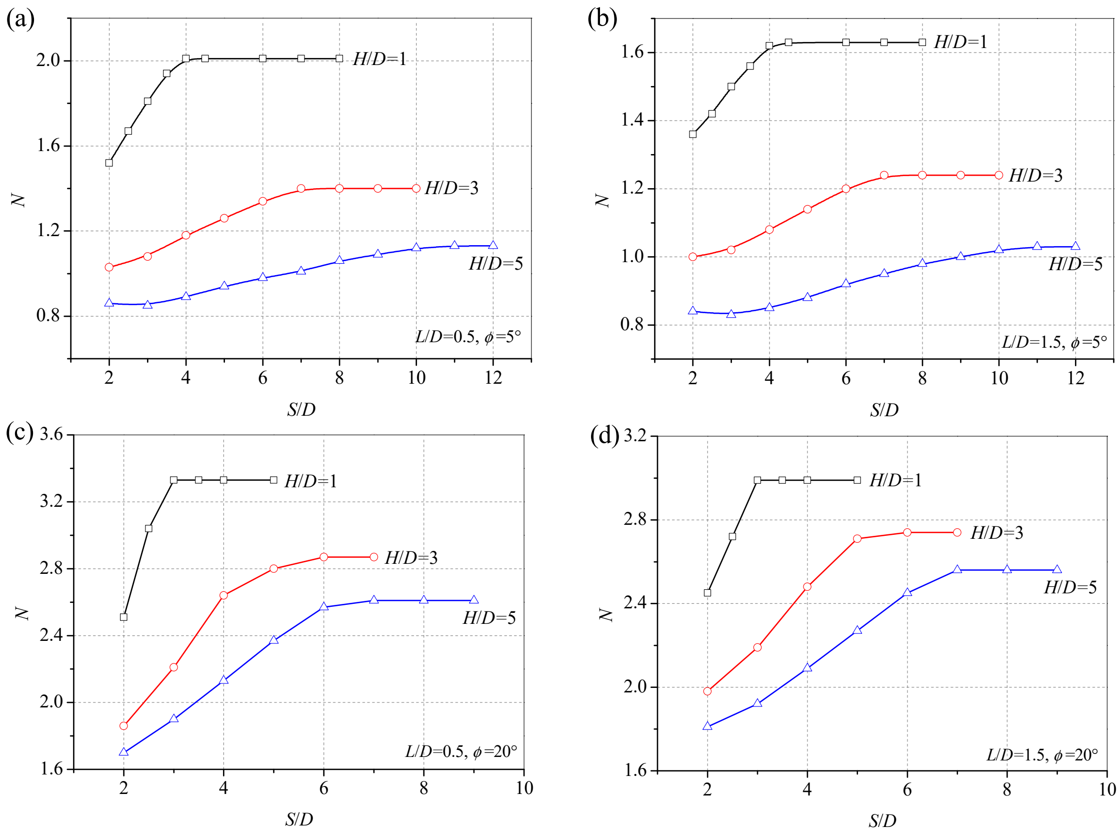


Figure 10. The variations of N with S/D and H/D for the case of R/D=1: (a) L/D=0.5, ϕ =5°, (b) L/D=1.5, ϕ =5°, (c) L/D=0.5, ϕ =20° and (d) L/D=1.5, ϕ =20°

($S_{cr}/D$), before reaching a maximum value of *N*. Secondly, as the value of *S*/*D* increases, the value of *N* initially decreases, then increases, and eventually becomes constant at a critical value of $S_{cr}/D$. It should be emphasized that when *S*/*D* is greater than or equal to $S_{cr}/D$, the stability number assumes a constant value, which is identical to that of a single isolated tunnel or void. This finding reveals that the center-to-center distance does not influence the value of *N*.

Fig. 9 displays the variations in *N* with *S*/*D* and highlights the impact of $\phi$. It is evident from the figure that an increase in the value of $\phi$ leads to a corresponding increase in *N*. Moreover, the rate of increase in *N* also increases with the value of $\phi$ increases. Additionally, the figure shows that a lower value of $\phi$ results in a higher value of $S_{cr}/D$, given constant values of *L*/*D* and *H*/*D*. For instance, in cases where *L*/*D*=0 and *H*/*D*=5, the values of $S_{cr}/D$ are 11, 9, 8, and 6 for $\phi$ = 5°, 10°, 15°, and 20°, respectively.

Fig. 10 presents the variation of *N* with *S*/*D* for different combinations of *H*/*D*. The figure indicates that a higher value of *H*/*D* results in a lower value of *N*. Additionally, the maximum stability number increases continuously with increasing *H*/*D*. The rate of increase in *N* with *S*/*D* is more significant for lower values of *H*/*D*. Meanwhile, the value of $S_{cr}/D$ increases with an increase in *H*/*D* and lies approximately in the range of 2.5-4 for *H*/*D* = 1, 5-7 for *H*/*D* = 3, and 7-12 for *H*/*D* = 5.

Table 2. Stability numbers of two circular tunnels with *R/D*=0.5

| *H/D* | *S/D* | $\phi$(°) | *L/D* 0 | 0.5 | 1 | 1.5 | 2 | $\phi$(°) | *L/D* 0 | 0.5 | 1 | 1.5 | 2 |
|---|---|---|---|---|---|---|---|---|---|---|---|---|---|
| 1 | 1.5 | 5 | 1.88 | 1.83 | 1.81 | 1.78 | 1.74 | 10 | 2.16 | 2.13 | 2.16 | 2.19 | 2.19 |
| | 2 | | 2.06 | 1.95 | 1.88 | 1.81 | 1.75 | | 2.44 | 2.34 | 2.29 | 2.26 | 2.22 |
| | 2.5 | | 2.24 | 2.11 | 1.99 | 1.88 | 1.80 | | 2.66 | 2.58 | 2.47 | 2.38 | 2.30 |
| | 3 | | 2.33 | 2.27 | 2.11 | 1.97 | 1.85 | | 2.67 | 2.67 | 2.64 | 2.52 | 2.40 |
| | 3.5 | | 2.33 | 2.33 | 2.24 | 2.07 | 1.92 | | 2.67 | 2.67 | 2.67 | 2.63 | 2.52 |
| | 4 | | 2.33 | 2.33 | 2.33 | 2.17 | 1.99 | | 2.67 | 2.67 | 2.67 | 2.67 | 2.67 |
| | 1.5 | 15 | 2.53 | 2.54 | 2.65 | 2.77 | 2.85 | 20 | 3.05 | 3.12 | 3.36 | 3.50 | 3.60 |
| | 2 | | 2.95 | 2.91 | 2.88 | 2.90 | 2.93 | | 3.60 | 3.60 | 3.60 | 3.60 | 3.60 |
| | 2.5 | | 3.07 | 3.07 | 3.07 | 3.07 | 3.00 | | 3.60 | 3.60 | 3.60 | 3.60 | 3.60 |
| | 3 | | 3.07 | 3.07 | 3.07 | 3.07 | 3.07 | | 3.60 | 3.60 | 3.60 | 3.60 | 3.60 |
| 3 | 1.5 | 5 | 1.24 | 1.24 | 1.24 | 1.26 | 1.26 | 10 | 1.50 | 1.50 | 1.53 | 1.57 | 1.60 |
| | 2 | | 1.26 | 1.25 | 1.24 | 1.25 | 1.24 | | 1.53 | 1.53 | 1.55 | 1.58 | 1.60 |
| | 3 | | 1.34 | 1.31 | 1.29 | 1.27 | 1.25 | | 1.68 | 1.65 | 1.65 | 1.64 | 1.64 |
| | 4 | | 1.42 | 1.39 | 1.36 | 1.33 | 1.29 | | 1.82 | 1.80 | 1.76 | 1.74 | 1.71 |
| | 5 | | 1.50 | 1.47 | 1.43 | 1.39 | 1.34 | | 1.85 | 1.85 | 1.85 | 1.85 | 1.85 |
| | 6 | | 1.51 | 1.51 | 1.49 | 1.45 | 1.40 | | 1.85 | 1.85 | 1.85 | 1.85 | 1.85 |
| | 1.5 | 15 | 1.84 | 1.86 | 1.94 | 2.03 | 2.13 | 20 | 2.33 | 2.42 | 2.57 | 2.75 | 2.90 |
| | 2 | | 1.93 | 1.94 | 2.01 | 2.07 | 2.14 | | 2.52 | 2.59 | 2.70 | 2.85 | 2.91 |
| | 3 | | 2.18 | 2.17 | 2.18 | 2.21 | 2.24 | | 2.94 | 2.93 | 2.92 | 2.94 | 2.94 |
| | 4 | | 2.31 | 2.31 | 2.31 | 2.31 | 2.31 | | 2.94 | 2.94 | 2.94 | 2.94 | 2.94 |
| | 5 | | 2.31 | 2.31 | 2.31 | 2.31 | 2.31 | | 2.94 | 2.94 | 2.94 | 2.94 | 2.94 |
| 5 | 1.5 | 5 | 1.02 | 1.01 | 1.01 | 1.01 | 1.01 | 10 | 1.26 | 1.26 | 1.27 | 1.29 | 1.32 |
| | 2 | | 1.01 | 1.00 | 1.00 | 1.00 | 1.00 | | 1.26 | 1.26 | 1.27 | 1.29 | 1.31 |
| | 3 | | 1.02 | 1.01 | 1.01 | 1.00 | 1.00 | | 1.31 | 1.30 | 1.31 | 1.32 | 1.32 |
| | 4 | | 1.06 | 1.04 | 1.03 | 1.02 | 1.01 | | 1.38 | 1.37 | 1.37 | 1.36 | 1.36 |
| | 5 | | 1.10 | 1.08 | 1.06 | 1.05 | 1.03 | | 1.45 | 1.44 | 1.43 | 1.42 | 1.40 |
| | 6 | | 1.14 | 1.12 | 1.12 | 1.08 | 1.06 | | 1.50 | 1.50 | 1.50 | 1.47 | 1.46 |
| | 7 | | 1.17 | 1.15 | 1.14 | 1.12 | 1.09 | | 1.50 | 1.50 | 1.50 | 1.50 | 1.50 |
| | 8 | | 1.18 | 1.18 | 1.17 | 1.15 | 1.12 | | 1.50 | 1.50 | 1.50 | 1.50 | 1.50 |
| | 1.5 | 15 | 1.61 | 1.63 | 1.67 | 1.73 | 1.79 | 20 | 2.13 | 2.19 | 2.30 | 2.43 | 2.55 |
| | 2 | | 1.65 | 1.66 | 1.70 | 1.74 | 1.80 | | 2.24 | 2.28 | 2.37 | 2.48 | 2.57 |
| | 3 | | 1.75 | 1.76 | 1.79 | 1.81 | 1.85 | | 2.48 | 2.51 | 2.56 | 2.62 | 2.65 |
| | 4 | | 1.89 | 1.89 | 1.89 | 1.91 | 1.92 | | 2.68 | 2.67 | 2.67 | 2.68 | 2.68 |
| | 5 | | 1.98 | 1.98 | 1.98 | 1.97 | 1.97 | | 2.68 | 2.68 | 2.68 | 2.68 | 2.68 |
| | 6 | | 1.99 | 1.99 | 1.99 | 1.99 | 1.99 | | 2.68 | 2.68 | 2.68 | 2.68 | 2.68 |

Fig. 11 illustrates the variations of $N$ with $S/D$ for different combinations of $R/D$, $H/D$ and $\phi$, where $L/D$ is held constant at 0.5. It is observed that, at a given value of $S/D$, $N$ decreases with an increase in $R/D$. Remarkably, as $R/D$ increases, the value of $S_{cr}/D$ initially increases, reaches a maximum value at $R/D$ = 1, and then decreases. For example, in cases where $H/D$ =5 and $\phi$ = 5°, as shown in Fig. 11(c), the stability number reaches a constant value approximately at $S_{cr}/D$ = 8 for $R/D$ =0.5, $S_{cr}/D$ = 11 for $R/D$ =1 and $S_{cr}/D$ = 9 for $R/D$ =1.5, respectively.

Table 3. Stability numbers of two circular tunnels with *R/D*=1

| *H/D* | *S/D* | $\phi$(°) | *L/D* | | | | | $\phi$(°) | *L/D* | | | | |
|---|---|---|---|---|---|---|---|---|---|---|---|---|---|
| | | | 0 | 0.5 | 1 | 1.5 | 2 | | 0 | 0.5 | 1 | 1.5 | 2 |
| 1 | 2 | 5 | 1.67 | 1.52 | 1.43 | 1.36 | 1.31 | 10 | 1.92 | 1.76 | 1.66 | 1.62 | 1.57 |
| | 2.5 | | 1.87 | 1.67 | 1.52 | 1.42 | 1.34 | | 2.22 | 1.98 | 1.82 | 1.71 | 1.63 |
| | 3 | | 2.08 | 1.81 | 1.63 | 1.50 | 1.39 | | 2.52 | 2.20 | 1.99 | 1.83 | 1.72 |
| | 3.5 | | 2.25 | 1.94 | 1.72 | 1.56 | 1.44 | | 2.60 | 2.35 | 2.12 | 1.94 | 1.80 |
| | 4 | | 2.31 | 2.01 | 1.80 | 1.62 | 1.49 | | 2.60 | 2.35 | 2.12 | 1.97 | 1.85 |
| | 4.5 | | 2.31 | 2.01 | 1.80 | 1.63 | 1.51 | | 2.60 | 2.35 | 2.12 | 1.97 | 1.85 |
| | 2 | 15 | 2.25 | 2.06 | 1.99 | 1.96 | 1.94 | 20 | 2.72 | 2.51 | 2.45 | 2.45 | 2.48 |
| | 2.5 | | 2.70 | 2.41 | 2.24 | 2.12 | 2.06 | | 3.34 | 3.04 | 2.84 | 2.72 | 2.64 |
| | 3 | | 3.03 | 2.73 | 2.49 | 2.32 | 2.20 | | 3.46 | 3.33 | 3.17 | 2.99 | 2.85 |
| | 3.5 | | 3.03 | 2.78 | 2.58 | 2.43 | 2.31 | | 3.46 | 3.33 | 3.17 | 2.99 | 2.93 |
| | 4 | | 3.03 | 2.78 | 2.58 | 2.43 | 2.31 | | 3.46 | 3.33 | 3.17 | 2.99 | 2.93 |
| 3 | 2 | 5 | 1.05 | 1.03 | 1.02 | 1.00 | 0.99 | 10 | 1.24 | 1.22 | 1.21 | 1.21 | 1.22 |
| | 3 | | 1.12 | 1.08 | 1.05 | 1.02 | 1.00 | | 1.37 | 1.32 | 1.28 | 1.26 | 1.24 |
| | 4 | | 1.24 | 1.18 | 1.13 | 1.08 | 1.04 | | 1.55 | 1.48 | 1.42 | 1.37 | 1.32 |
| | 5 | | 1.33 | 1.26 | 1.20 | 1.14 | 1.09 | | 1.72 | 1.62 | 1.55 | 1.47 | 1.41 |
| | 6 | | 1.43 | 1.34 | 1.26 | 1.20 | 1.13 | | 1.85 | 1.73 | 1.64 | 1.56 | 1.48 |
| | 7 | | 1.50 | 1.40 | 1.32 | 1.24 | 1.17 | | 1.85 | 1.75 | 1.66 | 1.58 | 1.51 |
| | 8 | | 1.50 | 1.40 | 1.32 | 1.24 | 1.18 | | 1.85 | 1.75 | 1.66 | 1.58 | 1.51 |
| | 2 | 15 | 1.49 | 1.48 | 1.49 | 1.52 | 1.54 | 20 | 1.87 | 1.86 | 1.91 | 1.98 | 2.04 |
| | 3 | | 1.73 | 1.67 | 1.64 | 1.62 | 1.61 | | 2.27 | 2.21 | 2.20 | 2.19 | 2.21 |
| | 4 | | 2.02 | 1.93 | 1.86 | 1.80 | 1.75 | | 2.76 | 2.64 | 2.52 | 2.48 | 2.43 |
| | 5 | | 2.28 | 2.16 | 2.04 | 1.97 | 1.89 | | 2.92 | 2.80 | 2.79 | 2.71 | 2.63 |
| | 6 | | 2.32 | 2.22 | 2.13 | 2.06 | 1.98 | | 2.92 | 2.87 | 2.79 | 2.74 | 2.68 |
| | 7 | | 2.32 | 2.22 | 2.13 | 2.06 | 1.98 | | 2.92 | 2.87 | 2.79 | 2.74 | 2.68 |
| 5 | 2 | 5 | 0.87 | 0.86 | 0.85 | 0.84 | 0.84 | 10 | 1.06 | 1.05 | 1.05 | 1.05 | 1.05 |
| | 3 | | 0.88 | 0.85 | 0.85 | 0.83 | 0.82 | | 1.09 | 1.07 | 1.06 | 1.05 | 1.05 |
| | 4 | | 0.92 | 0.89 | 0.87 | 0.85 | 0.84 | | 1.17 | 1.14 | 1.12 | 1.10 | 1.08 |
| | 5 | | 0.96 | 0.94 | 0.91 | 0.88 | 0.86 | | 1.25 | 1.21 | 1.18 | 1.15 | 1.12 |
| | 6 | | 1.01 | 0.98 | 0.94 | 0.92 | 0.89 | | 1.33 | 1.29 | 1.24 | 1.21 | 1.17 |
| | 7 | | 1.05 | 1.01 | 0.98 | 0.95 | 0.91 | | 1.41 | 1.36 | 1.31 | 1.27 | 1.22 |
| | 8 | | 1.10 | 1.06 | 1.01 | 0.98 | 0.94 | | 1.48 | 1.42 | 1.37 | 1.32 | 1.27 |
| | 9 | | 1.14 | 1.09 | 1.04 | 1.00 | 0.96 | | 1.51 | 1.46 | 1.40 | 1.35 | 1.31 |
| | 10 | | 1.17 | 1.12 | 1.07 | 1.02 | 0.98 | | 1.51 | 1.46 | 1.40 | 1.35 | 1.31 |
| | 11 | | 1.19 | 1.13 | 1.08 | 1.03 | 0.99 | | 1.51 | 1.46 | 1.40 | 1.35 | 1.31 |
| | 12 | | 1.19 | 1.13 | 1.08 | 1.03 | 0.99 | | 1.51 | 1.46 | 1.40 | 1.35 | 1.31 |
| | 2 | 15 | 1.32 | 1.31 | 1.32 | 1.35 | 1.37 | 20 | 1.70 | 1.70 | 1.74 | 1.81 | 1.87 |
| | 3 | | 1.40 | 1.38 | 1.38 | 1.38 | 1.39 | | 1.90 | 1.90 | 1.90 | 1.92 | 1.96 |
| | 4 | | 1.55 | 1.51 | 1.49 | 1.47 | 1.46 | | 2.16 | 2.13 | 2.11 | 2.09 | 2.10 |
| | 5 | | 1.69 | 1.65 | 1.61 | 1.57 | 1.55 | | 2.42 | 2.37 | 2.32 | 2.27 | 2.25 |
| | 6 | | 1.84 | 1.78 | 1.73 | 1.69 | 1.64 | | 2.63 | 2.57 | 2.51 | 2.45 | 2.41 |
| | 7 | | 1.95 | 1.89 | 1.83 | 1.78 | 1.73 | | 2.64 | 2.61 | 2.59 | 2.56 | 2.51 |
| | 8 | | 2.00 | 1.93 | 1.88 | 1.83 | 1.79 | | 2.64 | 2.61 | 2.59 | 2.56 | 2.51 |
| | 9 | | 2.00 | 1.93 | 1.88 | 1.83 | 1.79 | | 2.64 | 2.61 | 2.59 | 2.56 | 2.51 |

The plot depicted in Fig. 12 displays the variations of the stability number $N$ with respect to changes in $S/D$ for different combinations of $L/D$, $R/D$ and $\phi$. It is noteworthy that the $N$ values correspond to $H/D$ = 3 cases. Figs. 12(a) and 12(b) illustrate the cases of $R/D$ = 0.5. As the

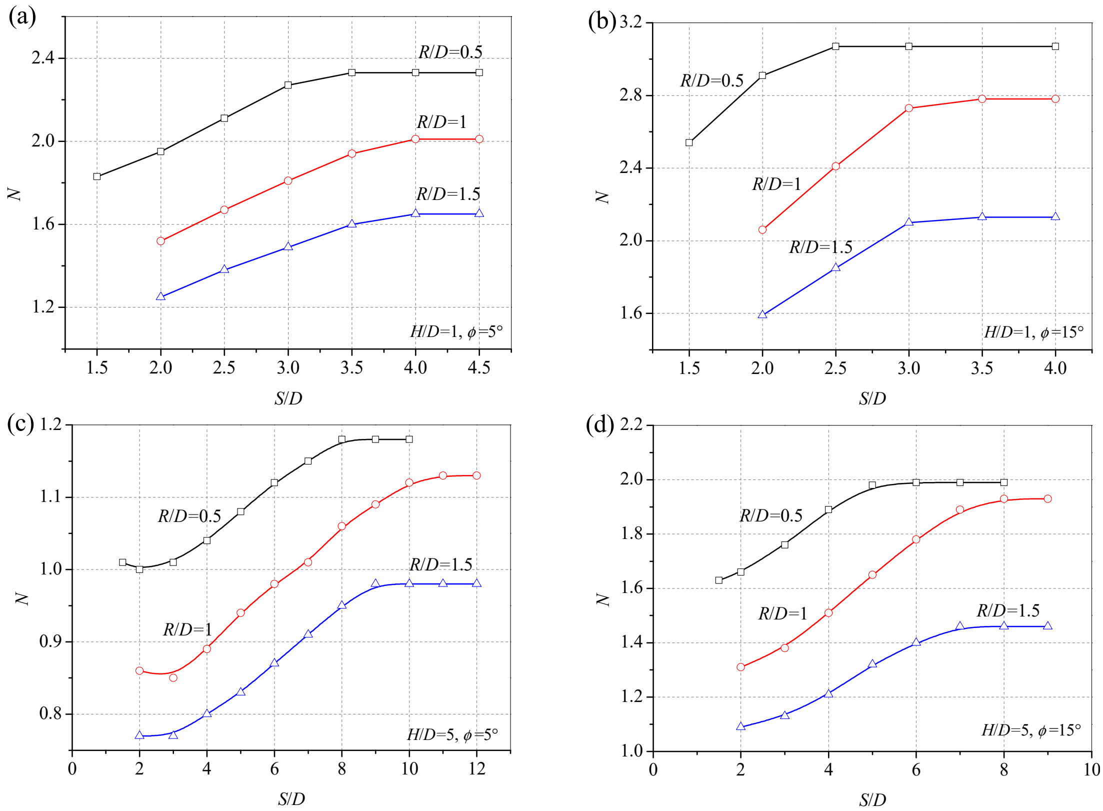


Figure 11. The variations of N with S/D and R/D for the case of L/D=0.5: (a) H/D=1, ϕ =5°, (b) H/D=1, ϕ =15°, (c) H/D=5, ϕ =5° and (d) H/D=5, ϕ =15°

stability number $N$ reaches a constant value, $L/D$ appears to have a negligible effect on the stability number.

However, for the instances of $R/D$ = 1.5 (Figs. 12(c) and 12(d)), the value of $N$ declines with the increase in $L/D$ when $S/D \geq S_{cr}/D$. This observation aligns with the failure mechanisms indicated in Fig. 15, where exceeding the critical value of $S_{cr}/D$ results in failure mechanisms identical to single tunnel A for $R/D$ = 0.5 and void B for $R/D$ = 1.5. For $S/D \leq S_{cr}/D$, various tendencies can be observed depending on the values of $R/D$ and $\phi$. For example, in the case of $R/D$ = 0.5 and $\phi$ = 10°, the value of $N$ increases as $L/D$ increases when $S/D \leq 2.5$. However, an opposite trend is observed when $2.5 \leq S/D \leq S_{cr}/D$, where $N$ decreases in magnitude as $L/D$ increases.

From a physical perspective, the dependence of the critical spacing ratio $S_{cr}/D$ on the problem parameters is fundamentally linked to the spatial evolution of the plastic shear zones. An increase in the soil friction angle $\phi$ enhances the soil's shear strength, resulting in steeper and more localized slip surfaces. This localization confines the horizontal extent of the failure mechanism, allowing the failure envelopes of the two cavities to decouple at a smaller horizontal distance, thereby reducing $S_{cr}/D$. Conversely, an increase in the depth ratio $H/D$ forces the failure mechanism to propagate through a thicker soil overburden. This extended propagation significantly enlarges the overall area of the slip surfaces, which promotes stress interference between the cavities even at larger horizontal distances, resulting in a higher $S_{cr}/D$.

Table 4. Stability numbers of two circular tunnels with *R/D*=1.5

| *H/D* | *S/D* | $\phi$(°) | *L/D* 0 | 0.5 | 1 | 1.5 | 2 | $\phi$(°) | *L/D* 0 | 0.5 | 1 | 1.5 | 2 |
|---|---|---|---|---|---|---|---|---|---|---|---|---|---|
| 1 | 2 | 5 | 1.37 | 1.25 | 1.17 | 1.12 | 1.08 | 10 | 1.53 | 1.40 | 1.32 | 1.29 | 1.25 |
| | 2.5 | | 1.55 | 1.38 | 1.25 | 1.16 | 1.10 | | 1.79 | 1.59 | 1.45 | 1.36 | 1.30 |
| | 3 | | 1.73 | 1.49 | 1.34 | 1.23 | 1.14 | | 2.05 | 1.74 | 1.56 | 1.45 | 1.36 |
| | 3.5 | | 1.90 | 1.60 | 1.41 | 1.28 | 1.18 | | 2.16 | 1.87 | 1.67 | 1.52 | 1.42 |
| | 4 | | 1.94 | 1.65 | 1.47 | 1.32 | 1.22 | | 2.16 | 1.87 | 1.69 | 1.56 | 1.46 |
| | 4.5 | | 1.94 | 1.65 | 1.47 | 1.32 | 1.22 | | 2.16 | 1.87 | 1.69 | 1.56 | 1.46 |
| | 2 | 15 | 1.73 | 1.59 | 1.52 | 1.51 | 1.49 | 20 | 2.02 | 1.85 | 1.79 | 1.79 | 1.81 |
| | 2.5 | | 2.10 | 1.85 | 1.71 | 1.64 | 1.57 | | 2.56 | 2.21 | 2.07 | 1.99 | 1.96 |
| | 3 | | 2.41 | 2.10 | 1.89 | 1.76 | 1.67 | | 2.72 | 2.46 | 2.30 | 2.17 | 2.07 |
| | 3.5 | | 2.41 | 2.13 | 1.97 | 1.85 | 1.74 | | 2.72 | 2.46 | 2.32 | 2.22 | 2.14 |
| | 4 | | 2.41 | 2.13 | 1.97 | 1.85 | 1.74 | | 2.72 | 2.46 | 2.32 | 2.22 | 2.14 |
| 3 | 2 | 5 | 0.92 | 0.89 | 0.87 | 0.86 | 0.85 | 10 | 1.05 | 1.02 | 1.01 | 1.01 | 1.01 |
| | 3 | | 0.98 | 0.93 | 0.89 | 0.87 | 0.85 | | 1.14 | 1.09 | 1.06 | 1.04 | 1.01 |
| | 4 | | 1.05 | 1.00 | 0.95 | 0.91 | 0.87 | | 1.28 | 1.21 | 1.15 | 1.11 | 1.07 |
| | 5 | | 1.14 | 1.06 | 1.00 | 0.96 | 0.91 | | 1.41 | 1.32 | 1.25 | 1.20 | 1.14 |
| | 6 | | 1.20 | 1.13 | 1.06 | 1.00 | 0.95 | | 1.47 | 1.38 | 1.31 | 1.25 | 1.19 |
| | 7 | | 1.24 | 1.16 | 1.09 | 1.03 | 0.98 | | 1.47 | 1.38 | 1.31 | 1.26 | 1.20 |
| | 8 | | 1.24 | 1.16 | 1.09 | 1.03 | 0.98 | | 1.47 | 1.38 | 1.31 | 1.26 | 1.20 |
| | 2 | 15 | 1.22 | 1.20 | 1.20 | 1.22 | 1.23 | 20 | 1.46 | 1.45 | 1.47 | 1.50 | 1.55 |
| | 3 | | 1.39 | 1.33 | 1.29 | 1.27 | 1.26 | | 1.74 | 1.68 | 1.65 | 1.63 | 1.64 |
| | 4 | | 1.60 | 1.52 | 1.45 | 1.41 | 1.36 | | 2.08 | 1.97 | 1.90 | 1.83 | 1.79 |
| | 5 | | 1.76 | 1.69 | 1.59 | 1.52 | 1.46 | | 2.15 | 2.08 | 2.02 | 1.98 | 1.94 |
| | 6 | | 1.76 | 1.69 | 1.62 | 1.56 | 1.51 | | 2.15 | 2.08 | 2.02 | 1.98 | 1.94 |
| | 7 | | 1.76 | 1.69 | 1.62 | 1.56 | 1.51 | | 2.15 | 2.08 | 2.02 | 1.98 | 1.94 |
| 5 | 2 | 5 | 0.77 | 0.76 | 0.75 | 0.74 | 0.74 | 10 | 0.91 | 0.90 | 0.89 | 0.89 | 0.89 |
| | 3 | | 0.77 | 0.75 | 0.74 | 0.72 | 0.71 | | 0.92 | 0.90 | 0.89 | 0.88 | 0.87 |
| | 4 | | 0.80 | 0.77 | 0.75 | 0.73 | 0.72 | | 0.98 | 0.95 | 0.92 | 0.91 | 0.89 |
| | 5 | | 0.83 | 0.80 | 0.77 | 0.76 | 0.73 | | 1.05 | 1.01 | 0.98 | 0.95 | 0.93 |
| | 6 | | 0.87 | 0.84 | 0.81 | 0.78 | 0.76 | | 1.11 | 1.07 | 1.03 | 1.00 | 0.97 |
| | 7 | | 0.91 | 0.87 | 0.84 | 0.81 | 0.78 | | 1.18 | 1.13 | 1.08 | 1.04 | 1.01 |
| | 8 | | 0.95 | 0.90 | 0.86 | 0.83 | 0.80 | | 1.21 | 1.16 | 1.12 | 1.08 | 1.04 |
| | 9 | | 0.98 | 0.93 | 0.89 | 0.85 | 0.82 | | 1.21 | 1.16 | 1.12 | 1.08 | 1.05 |
| | 10 | | 0.98 | 0.94 | 0.89 | 0.86 | 0.83 | | 1.21 | 1.16 | 1.12 | 1.08 | 1.05 |
| | 11 | | 0.98 | 0.94 | 0.89 | 0.86 | 0.83 | | 1.21 | 1.16 | 1.12 | 1.08 | 1.05 |
| | 2 | 15 | 1.10 | 1.09 | 1.10 | 1.11 | 1.12 | 20 | 1.35 | 1.35 | 1.37 | 1.41 | 1.45 |
| | 3 | | 1.15 | 1.13 | 1.12 | 1.11 | 1.11 | | 1.49 | 1.46 | 1.46 | 1.49 | 1.48 |
| | 4 | | 1.25 | 1.21 | 1.19 | 1.17 | 1.15 | | 1.67 | 1.62 | 1.59 | 1.57 | 1.56 |
| | 5 | | 1.36 | 1.32 | 1.28 | 1.25 | 1.22 | | 1.85 | 1.79 | 1.74 | 1.70 | 1.67 |
| | 6 | | 1.47 | 1.40 | 1.36 | 1.32 | 1.29 | | 1.95 | 1.91 | 1.85 | 1.80 | 1.76 |
| | 7 | | 1.51 | 1.46 | 1.42 | 1.38 | 1.34 | | 1.95 | 1.91 | 1.87 | 1.84 | 1.81 |
| | 8 | | 1.51 | 1.46 | 1.42 | 1.40 | 1.36 | | 1.95 | 1.91 | 1.87 | 1.84 | 1.81 |
| | 9 | | 1.51 | 1.46 | 1.42 | 1.40 | 1.36 | | 1.95 | 1.91 | 1.87 | 1.84 | 1.81 |

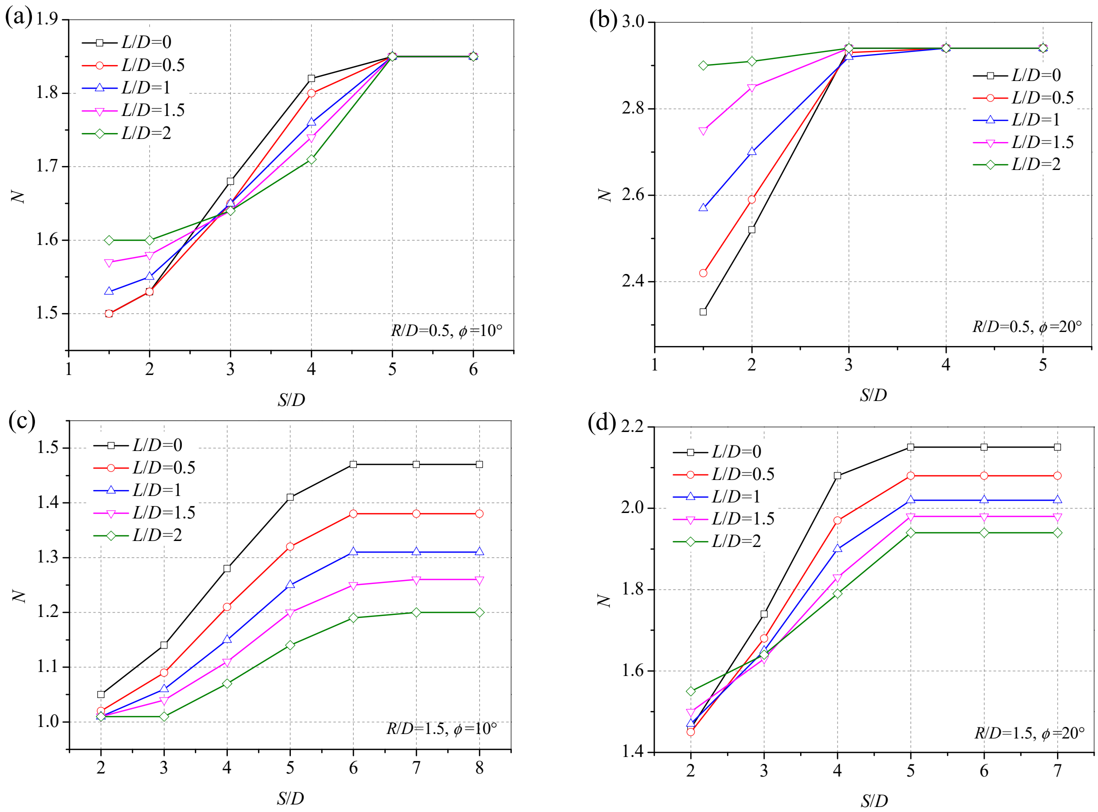


Figure 12. The variations of N with S/D and L/D for the case of H/D=3: (a) R/D=0.5, ϕ =10°, (b) R/D=0.5, ϕ =20°, (c) R/D=1.5, ϕ =10° and (d) R/D=1.5, ϕ =20°

Furthermore, the diameter ratio $R/D$ governs the geometric dominance of the interacting stress fields. When $R/D = 1$, the structural symmetry maximizes the mutual interference between the cavities, yielding the maximum $S_{cr}/D$. Deviations from this symmetric ratio shift the failure dominance toward the larger cavity, effectively reducing the interactive influence range and thus decreasing the critical spacing.

## 5.3 Failure mechanisms

Fig. 13 illustrates the UB failure mechanisms with the influence of $S/D$ for the $\phi$ values of 5° and 20°. As presented in Figs. 13(a)-13(c), the failure mechanisms comprise two components, namely a cross-shaped zone between the voids and two larger slip surfaces that extend from the voids to the ground surface. For the cases of $\phi$ = 5°, the size of the cross-shaped zone increases with the increase in $S/D$, and the cross-shaped area tends to vanish as $S/D$ reaches 7, indicating no interaction between the voids. This observation clarifies the phenomenon where the stability number becomes constant at a critical value of $S_{cr}/D$. Moreover, Fig. 13(b) shows that the cross-shaped zone's size for $\phi$ = 20° is larger than that for $\phi$ = 5° [(Fig. 13(a)]. Remarkably, for $\phi$ = 20°, only single void B fails as $S/D$ increases to 5, suggesting that a higher value of $\phi$ corresponds to a lower magnitude of $S_{cr}/D$, as corroborated by Fig. 9.

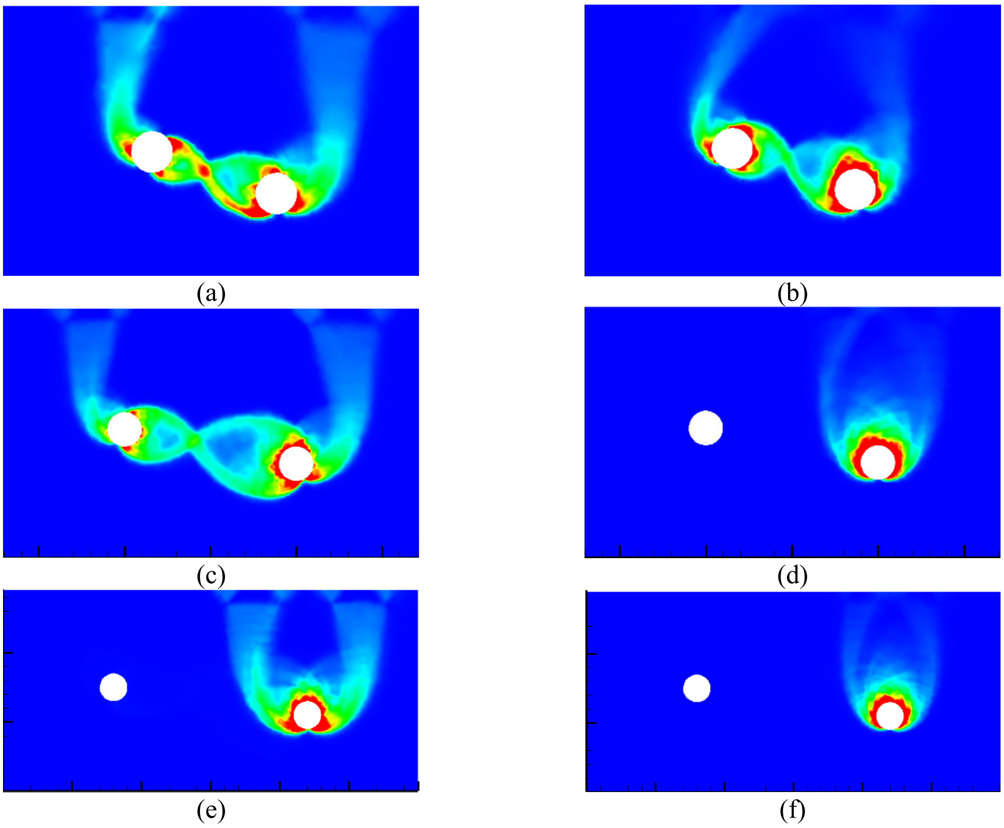

Figure 13. Upper bound failure mechanisms (H/D=3, R/D=1 and L/D=1): (a) S/D=3, ϕ=5°, (b) S/D=3, ϕ=20°, (c) S/D=5, ϕ=5°, (d) S/D=5, ϕ=20°, (e) S/D=7, ϕ=5° and (f) S/D=7, ϕ=20°

In Fig. 14, UB failure mechanisms are presented for various *H*/*D* ratios, with *S*/*D* ratios of 2 and 4. The cases for *S*/*D* = 2, depicted in Figs. 14(a), 14(c), and 14(e), reveal that an increase in *H*/*D* ratio results in an expansion of the slip surface area while the cross-shaped zone's size remains constant. The trend is similar for the cases of *S*/*D* = 4, except for the instance of *H*/*D* =1, as shown in Fig. 14(b), where only void B experiences failure. This observation suggests that $S_{cr}/D$ magnitude decreases with an increase in *H*/*D* ratio.

Fig. 15 shows the UB failure mechanisms for various *S*/*D* ratios at *R*/*D* values of 0.5 and 1.5. For *R*/*D* = 0.5, a larger wedge-shaped zone is evident near tunnel A compared to those near void B. Conversely, for *R*/*D* = 1.5, the wedge-shaped zone near tunnel A is smaller than that near void B. When *S*/*D* = 6, only tunnel A fails for *R*/*D* = 0.5, whereas only void B fails for *R*/*D* = 1.5. Moreover, an increase in *S*/*D* and *R*/*D* values leads to an expansion in the size of the cross-shaped zone and two slip surfaces.

The impact of *L*/*D* on UB failure mechanisms is demonstrated in Fig. 16 for the cases of *R*/*D* = 0.5 and 1.5. As *L*/*D* increases, the wedge-shaped zone near void B tends to enlarge, while the wedge-shaped area adjacent to tunnel A rotates downward with no significant change in size. Furthermore, an increase in *R*/*D* and *L*/*D* values results in an expansion of the plastic zone. In the case of *R*/*D* = 0.5, both the top and bottom of tunnel A and void B are prone to damage, while for *R*/*D* = 1.5, only the side of tunnel A and void B may incur damage.

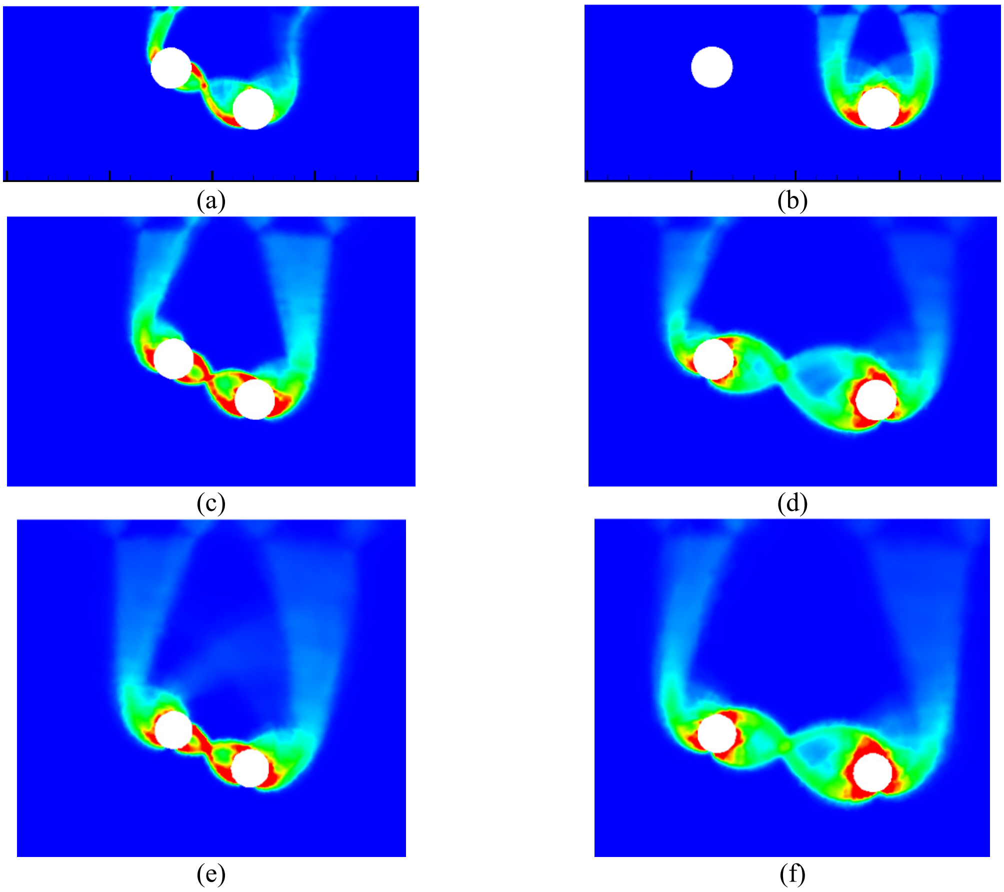


Figure 14. Upper bound failure mechanisms (R/D=1, L/D=1 and $\phi$=10°): (a) H/D=1, S/D=2, (b) H/D=1, S/D=4, (c) H/D=3, S/D=2, (d) H/D=3, S/D=4, (e) H/D=5, S/D=2 and (f) H/D=5, S/D=4

Overall, the main trends of the stability number $N$ discussed in Section 5.2 are kinematically governed by the evolution of these failure mechanisms. When $S/D < S_{cr}/D$, the strong interaction between the two cavities is characterized by the formation of the cross-shaped plastic zone (as seen in Figs. 13-15). This mutual stress interference significantly reduces the overall stability $N$. However, as $S/D$ reaches the critical value $S_{cr}/D$, this cross-shaped zone completely vanishes, indicating spatial decoupling. The failure mechanism transitions into isolated local failures (dominated by either tunnel A or void B alone), which perfectly explains why the stability number $N$ ceases to increase and remains constant beyond this point.

Furthermore, the localized slip surfaces caused by a higher friction angle $\phi$ (Fig. 13) limit the expansion of the interactive zone, allowing the cavities to decouple at smaller spacings and rapidly stabilizing $N$. Conversely, deeper tunnels with higher $H/D$ ratios (Fig. 14) generate more extensive slip surfaces that merge more easily, providing a clear kinematic justification for the overall lower stability numbers and the delayed decoupling (i.e., larger $S_{cr}/D$). Finally, the expansion and rotation of the failure wedges observed in Fig. 16 visually account for the reduction in $N$ as $L/D$ or $R/D$ increases.

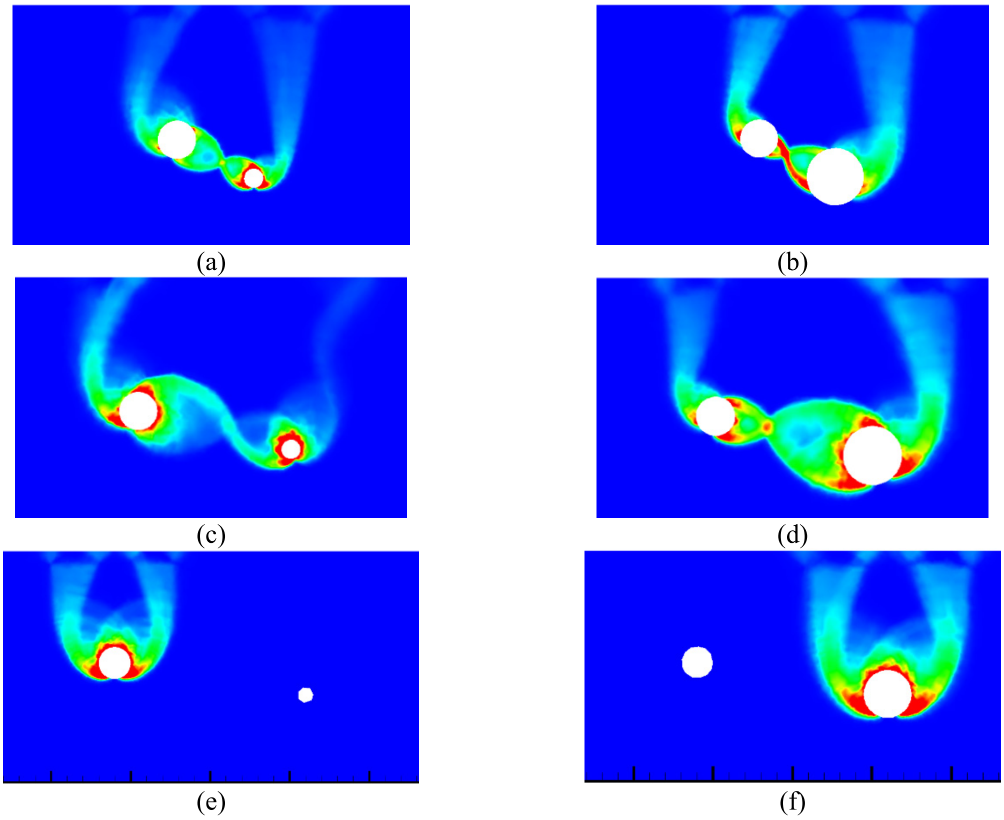

Figure 15. Upper bound failure mechanisms (H/D=3, L/D=1 and $\phi$=10°): (a) R/D=0.5, S/D=2, (b) R/D=1.5, S/D=2, (c) R/D=0.5, S/D=4, (d) R/D=1.5, S/D=4, (e) R/D=0.5, S/D=6 and (f) R/D=1.5, S/D=6

## 5.4 Practical applicability and limitations

The design tables and charts presented in this study provide a high-efficiency reference for the preliminary stability assessment of tunnels near voids. However, their application should consider the following boundary conditions:

(1) Geometric conditions: The results are based on the plane strain assumption, which is most reliable for the long-distance sections of tunnels. For regions dominated by three-dimensional effects, such as the tunnel face or complex junctions, supplementary 3D analyses are recommended.

(2) Geological conditions: The assumption of a homogeneous and isotropic soil layer serves as a theoretical baseline. In projects involving highly stratified or anisotropic ground, the stability number $N$ should be adjusted based on the properties of the weakest layer or site-specific conditions.

(3) Flow rule: This study adopts the associated flow rule ($\psi = \phi$) to maintain the rigor of the FELA framework. Since real soils often exhibit non-associated behavior ($\psi < \phi$), the stability numbers reported here represent an idealized upper-bound scenario. Practitioners are advised to incorporate an appropriate factor of safety (FS) when applying these results to sensitive or highly dilatant soils.

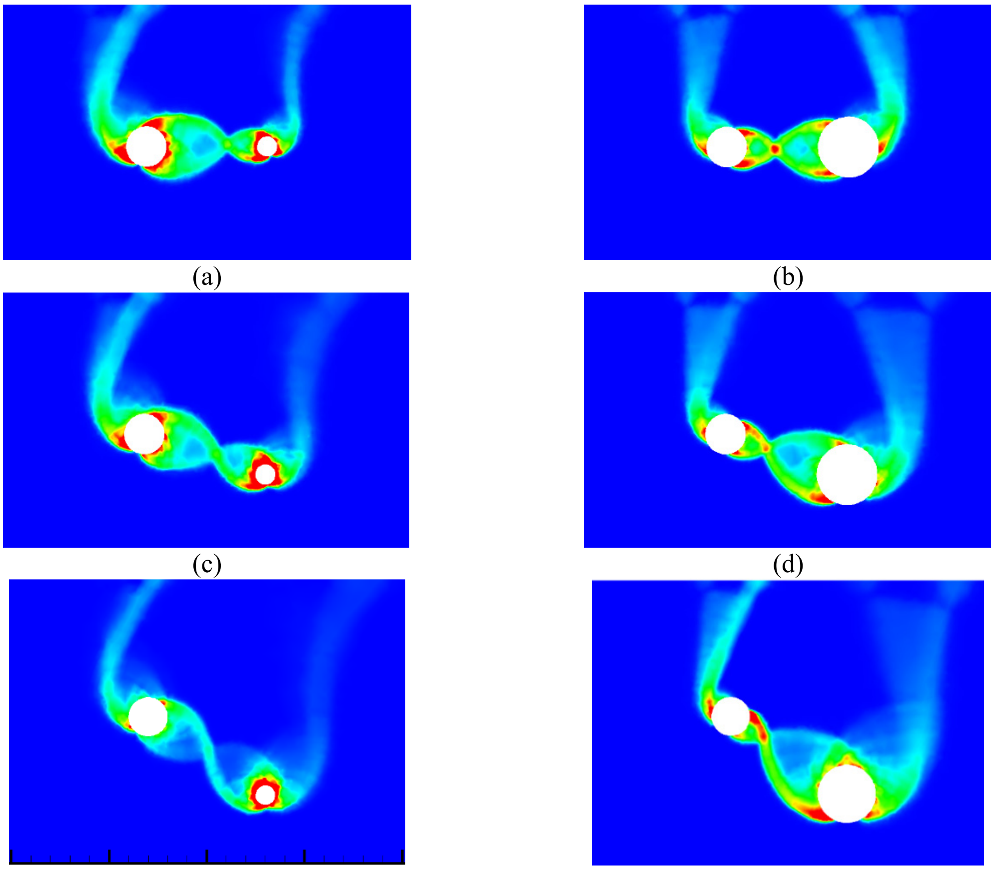

(a) (b) (c) (d) (e) (f)

Figure 16. Upper bound failure mechanisms (H/D=3, S/D=3 and ϕ=10°): (a) R/D=0.5, L/D=0, (b) R/D=1.5, L/D=0, (c) R/D=0.5, L/D=1, (d) R/D=1.5, L/D=1, (e) R/D=0.5, L/D=2 and (f) R/D=1.5, L/D=2

## 6. Conclusions

An investigation was conducted on the stability of a circular tunnel constructed in soil with a circular void. The adaptive FELA method, in combination with the NLP algorithm, was employed. Based on the FAIPA technique, a new imprecise step search algorithm was proposed to improve the computational efficiency of the NLP algorithm. The study calculated rigorous upper and lower bounds of the dimensionless stability number $N$, and the relative errors between them were found to be within 4% or better. The results were presented in design tables and charts, and the influence of material properties and geometric parameters on the stability number and failure mechanisms were discussed. Based on the FELA results of the present study, the following conclusions can be drawn:

(1) Generally, the stability number increases with an increase in the values of the center-to-center distance ratio $S/D$ and soil friction angle $\phi$, and decreases with increasing tunnel depth-to-diameter ratio $H/D$. A certain critical value of $S_{cr}/D$ was identified, at which the stability number reaches a constant value, indicating that the center-to-center distance has a negligible effect on the stability number.

(2) The value of $S_{cr}/D$ decreases with increasing $\phi$, and increases with an increase in the value of $H/D$. As the value of $R/D$ increases, the magnitude of $S_{cr}/D$ first increases, then decreases, and the maximum value of $S_{cr}/D$ is reached at $R/D = 1$. The parameter $L/D$ has little effect on the value of $S_{cr}/D$.
(3) When $S/D \geq S_{cr}/D$, the stability number is unaffected by the value of $L/D$ for the cases with lower values of $R/D$, and the value of $N$ decreases with increasing $L/D$ for the cases with greater values of $R/D$.
(4) When $S/D<S_{cr}/D$, the failure mechanism consists of a cross-shaped zone between two tunnels and two larger slip surfaces developed from the outside of the tunnels to the ground surface. When $S/D \geq S_{cr}/D$, the failure mechanism becomes that of only a single tunnel A or void B, which mainly depends on the parameters $R/D$ and $L/D$.

## Acknowledgements

The authors would like to acknowledge the financial support of the National Natural Science Foundation of China (Nos. 52468046, 52108316, 42407279), the Excellent Youth Project of Hunan Provincial Department of Education (Nos. 23B0806, 25B0809), the General Project of Hunan Provincial Department of Education (No. 24C0511),the Hunan Provincial Natural Science Foundation(No. 2025JJ80012) ,which made the work presented in this paper possible.

## References

1. Davis, E.H., Gunn, M.J., Mair, R.J., Seneviratine, H.N. (1980). The stability of shallow tunnels and underground openings in cohesive material. Geotechnique, 30(4), 397-416. https://doi.org/10.1680/geot.1980.30.4.397.
2. Leca, E., Dormieux, L. (1990). Upper and lower bound solutions for the face stability of shallow circular tunnels in frictional material. Geotechnique, 40(4), 581-606. https://doi.org/10.1680/geot.1990.40.4.581.
3. Osman, A.S, Mair, R.J, Bolton, M.D. (2006). On the kinematics of 2D tunnel collapse in undrained clay. Geotechnique, 56(9), 585-595. https://doi.org/10.1680/geot.2006.56.9.585.
4. Pan, Q., Chen, Z., Wu, Y., Dias, D., Oreste, P. (2021). Probabilistic tunnel face stability analysis: A comparison between LEM and LAM. Geomechanics and Engineering, 24(4), 399-406. https://doi.org/10.12989/gae.2021.24.4.399.
5. Sloan, S.W., Assadi, A. (1993). Stability of shallow tunnels in soft ground. Predictive soil mechanics. Thomas Telford, London, United Kingdom. https://doi.org/10.1680/psm.19164.0040.
6. Wilson, D.W., Abbo, A.J., Sloan, S.W., Lyamin, A.V. (2011). Undrained stability of a circular tunnel where the shear strength increases linearly with depth. Canadian Geotechnical Journal, 48(9), 1328-1342. https://doi.org/10.1139/t11-041.
7. Wilson, D.W., Abbo, A.J., Sloan, S.W., Lyamin, A.V. (2013). Undrained stability of a square tunnel where the shear strength increases linearly with depth. Computers and Geotechnics, 49, 314-325. https://doi.org/10.1016/j.compgeo.2012.09.005.
8. Abbo, A.J., Wilson, D.W., Sloan, S.W., Lyamin, A.V. (2013). Undrained stability of wide rectangular tunnels. Computers and Geotechnics, 53, 46-59. https://doi.org/10.1016/j.compgeo.2013.04.005.
9. Yamamoto, K., Lyamin, A.V., Wilson, D.W., Sloan, S.W., Abbo, A.J. (2011). Stability of a circular tunnel in cohesive-frictional soil subjected to surcharge loading. Computers and Geotechnics, 38(4), 504-514. https://doi.org/10.1016/j.compgeo.2011.02.014.

10. Yang, F., Sun, X., Zheng, X., Yang, J. (2016). Stability analysis of a deep buried elliptical tunnel in cohesive–frictional ($c$–$\phi$) soils with a nonassociated flow rule. Canadian Geotechnical Journal, 54(5), 736-741. https://doi.org/10.1139/cgj-2016-0523.
11. Zhang, R., Chen, G., Zou, J., Zhao, L., Jiang, C. (2019). Study on roof collapse of deep circular cavities in jointed rock masses using adaptive finite element limit analysis. Computers and Geotechnics, 111, 42-55. https://doi.org/10.1016/j.compgeo.2019.03.003.
12. Pandey, S., Tyagi, A. (2023). Stability of rectangular tunnel in improved soil surrounded by soft clay. Geomechanics and Engineering, 34(5), 491-505. https://doi.org/10.12989/gae.2023.34.5.491.
13. Kumar, B., Sahoo, J.P. (2023). Stability assessment of unlined tunnels with semicircular arch and straight sides in anisotropic clay. Geomechanics and Engineering, 35(2), 149-163. https://doi.org/10.12989/gae.2023.35.2.149.
14. Kim, D. (2024). Structural stability evaluation of TBM tunnels using numerical analysis approach. Geomechanics and Engineering, 38(6), 583-591. https://doi.org/10.12989/gae.2024.38.6.583.
15. Soliman, E., Duddeck, H., Ahrens, H. (1993). Two-and three-dimensional analysis of closely spaced double-tube tunnels. Tunnelling and Underground Space Technology, 8(1), 13-18. https://doi.org/10.1016/0886-7798(93)90130-N.
16. Yamamoto, K., Lyamin, A.V., Wilson, D.W., Sloan, S.W., Abbo, A.J. (2013). Stability of dual circular tunnels in cohesive-frictional soil subjected to surcharge loading. Computers and Geotechnics, 50, 41-54. https://doi.org/10.1016/j.compgeo.2012.12.008.
17. Yamamoto, K., Lyamin, A.V., Wilson, D.W., Sloan, S.W., Abbo, A.J. (2014). Stability of dual square tunnels in cohesive-frictional soil subjected to surcharge loading. Canadian Geotechnical Journal, 51(8), 829-843. https://doi.org/10.1139/cgj-2013-0481.
18. Wilson, D.W., Abbo, A.J., Sloan, S.W., Lyamin, A.V. (2014). Undrained stability of dual circular tunnels. International Journal of Geomechanics, 14(1), 69-79. https://doi.org/10.1061/(ASCE)GM.1943-5622.0000288.
19. Wilson, D.W., Abbo, A.J., Sloan, S.W., Lyamin, A.V. (2015). Undrained stability of dual square tunnels. Acta Geotechnica, 10(5), 665-682. https://doi.org/10.1007/s11440-014-0340-1.
20. Liu, X., Suliman, L., Zhou, X., Zhang, J., Xu, B. (2022). The difference in the slope supported system when excavating twin tunnels: Model test and numerical simulation. Geomechanics and Engineering, 31(1), 15-30. https://doi.org/10.12989/gae.2022.31.1.015.
21. Kim, S.H., Burd, H.J., Milligan, G.W.E. (1998). Model testing of closely spaced tunnels in clay. Geotechnique, 48(3), 375-388. https://doi.org/10.1680/geot.1998.48.3.375.
22. Wu, B.R., Lee, C.J. (2003). Ground movements and collapse mechanisms induced by tunneling in clayey soil. International Journal of Physical Modelling in Geotechnics, 3(4), 15-29. https://doi.org/10.1680/ijpmg.2003.030402.
23. Lee, C.J., Wu, B.R., Chen, H.T., Chiang, K.H. (2006). Tunnel stability and arching effects during tunneling in soft clayey soil. Tunnelling and Underground Space Technology, 21(2), 119-132. https://doi.org/10.1016/j.tust.2005.06.003.
24. Zhang, C.Y., Yu, C.H., Leung, A.K., Mohammad, S., Choi, C.E. (2025). Uprooting dynamics of a model tree under rockfall impact: Combined experimental and numerical insights. Earth Surface Processes and Landforms, 50(9), e70114. https://doi.org/10.1002/esp.70114.
25. Zhang, C.Y., Yin, Y.P., Zhang, M., Liao, D. (2024). Failure and reinforcement of reservoir landslides: insights from centrifuge modeling and numerical modeling. Engineering Geology, 343, 107806. https://doi.org/10.1016/j.enggeo.2024.107806.
26. Zhang, C.Y., Yin, Y.P., Yan, H., Zhu, S.N., Zhang, M., Wang, L.Q. (2024). Centrifuge modeling of unreinforced and multi-row stabilizing piles reinforced landslides subjected to reservoir water level fluctuation. Journal of Rock Mechanics and Geotechnical Engineering, 16(5), 1600-1614. https://doi.org/10.1016/j.jrmge.2023.09.025.
27. Osman, A.S. (2010). Stability of unlined twin tunnels in undrained clay. Tunnelling and Underground Space Technology, 25(3), 290-296. https://doi.org/10.1016/j.tust.2010.01.004.
28. Sahoo, J.P., Kumar, J. (2013). Stability of long unsupported twin circular tunnels in soils. Tunnelling

and Underground Space Technology, 38, 326-335. https://doi.org/10.1016/j.tust.2013.07.005.
29. Sahoo, J.P., Kumar, J. (2018). Required lining pressure for the stability of twin circular tunnels in soils. International Journal of Geomechanics, 18(7), 04018069. https://doi.org/10.1061/(ASCE)GM.1943-5622.0001196.
30. Yang, F., Zheng, X., Zhang, J., Yang, J. (2017). Upper bound analysis of stability of dual circular tunnels subjected to surcharge loading in cohesive-frictional soils. Tunnelling and Underground Space Technology, 61, 150-160. https://doi.org/10.1016/j.tust.2016.10.006.
31. Zhang, J., Yang, F., Yang, J., Zheng, X., Zeng, F. (2016). Upper-bound stability analysis of dual unlined elliptical tunnels in cohesive-frictional soils. Computers and Geotechnics, 80, 283-289. https://doi.org/10.1016/j.compgeo.2016.08.023.
32. Zhang, J., Feng, T., Yang, J., Yang, F., Gao, Y. (2018). Upper-bound stability analysis of dual unlined horseshoe-shaped tunnels subjected to gravity. Computers and Geotechnics, 97, 103-110. https://doi.org/10.1016/j.compgeo.2018.01.006.
33. Zhang, R., Xiao, Y., Zhao, M., Zhao, H. (2019). Stability of dual circular tunnels in a rock mass subjected to surcharge loading. Computers and Geotechnics, 108, 257-268. https://doi.org/10.1016/j.compgeo.2019.01.004.
34. Xiao, Y., Zhao, M., Zhang, R., Zhao, H., Wu, G. (2019). Stability of dual square tunnels in rock masses subjected to surcharge loading. Tunnelling and Underground Space Technology, 92, 103037. https://doi.org/10.1016/j.tust.2019.103037.
35. Rahaman, O., Kumar, J. (2020). Stability analysis of twin horse-shoe shaped tunnels in rock mass. Tunnelling and Underground Space Technology, 98, 103354. https://doi.org/10.1016/j.tust.2020.103354.
36. Zaid, M. (2021). Three-dimensional finite element analysis of urban rock tunnel under static loading condition: Effect of the rock weathering. Geomechanics and Engineering, 25(2), 99-109. https://doi.org/10.12989/gae.2021.25.2.099.
37. Chehade, F.H., Shahrour, I. (2008). Numerical analysis of the interaction between twin-tunnels: Influence of the relative position and construction procedure. Tunnelling and Underground Space Technology, 23(2), 210-214. https://doi.org/10.1061/j.tust.2007.03.004.
38. Banerjee, S.K., Chakraborty, D. (2018). Behavior of twin tunnels under different physical conditions. International Journal of Geomechanics, 18(8), 06018018. https://doi.org/10.1061/(ASCE)GM.1943-5622.0001216.
39. Xiao, Y., Zhao, M., Zhang, R., Zhao, H., Peng, W. (2019). Stability of two circular tunnels at different depths in cohesive-frictional soils subjected to surcharge loading. Computers and Geotechnics, 112, 23-34. https://doi.org/10.1016/j.compgeo.2019.04.006.
40. La, Y., Kim, B. (2020). Stability evaluation of a double-deck tunnel with diverging section. Geomechanics and Engineering, 21(2), 123-132. https://doi.org/10.12989/gae.2020.21.2.123.
41. Zhang, R. (2015). Finite element limit analysis based on non-linear programming and its applications in engineering. Ph.D. Dissertation, Hunan University, Changsha, China.
42. Zhang, R. (2019). Study on algorithms for adaptive finite element limit analysis method and its applications to complex geotechnical stability problems. Central South University, Changsha, China.
43. Sloan, S.W. (2013). Geotechnical stability analysis. Geotechnique, 63(7), 531-572. https://doi.org/10.1680/geot.12.RL.001.
44. Lyamin, A.V., Krabbenhøft, K., Abbo, A.J., Sloan, S.W. (2005). General approach to modelling discontinuities in limit analysis. Proceedings of the 11th International Conference of the International Association for Computer Methods and Advances in Geomechanics, Torino, Italy, June.
45. Krabbenhoft, K., Lyamin, A.V., Hjiaj, M., Sloan, S.W. (2005). A new discontinuous upper bound limit analysis formulation. International Journal for Numerical Methods in Engineering, 63, 1069-1088. https://doi.org/10.1002/nme.1314.
46. Zouain, N., Herskovits, J., Borges, L.A., Feijoo, R.A. (1993). An iterative algorithm for limit analysis with nonlinear yield functions. International Journal of Solids and Structures, 30(10), 1397-1417. https://doi.org/10.1016/0020-7683(93)90220-2.

47. Borges, L.A., Zouain, N., Huespe, A.E. (1996). A nonlinear optimization procedure for limit analysis. European Journal of Mechanics-A/Solids, 15(3), 487-512.
48. Lyamin, A.V., Sloan, S.W. (2002). Lower bound limit analysis using non-linear programming. International Journal for Numerical Methods in Engineering, 55(5), 573-611. https://doi.org/10.1002/nme.511.
49. Lyamin, A.V., Sloan, S.W. (2002). Upper bound limit analysis using linear finite elements and non-linear programming. International Journal for Numerical and Analytical Methods in Geomechanics, 26(2), 181-216. https://doi.org/10.1002/nag.198.
50. Krabbenhøft, K., Lyamin, A.V., Sloan, S.W. (2007). Formulation and solution of some plasticity problems as conic programs. Inteternatioal Journal of Solids and Structures, 44(5), 1533-1549. https://doi.org/10.1016/j.ijsolstr.2006.06.036.
51. Krabbenhøft, K., Lyamin, A.V., Sloan, S.W. (2008). Three dimensional Mohr-Coulomb limit analysis using semidefinite programming. Communications in Numerical Methods Engineering, 24(11), 1107-1119. https://doi.org/10.1002/cnm.1018.
52. Herskovits, J., Mappa, P., Goulart, E., Soares, C.M. (2005). Mathematical programming models and algorithms for engineering design optimization. Computer Methods in Applied Mechanics and Engineering, 194(30-33), 3244-3268. https://doi.org/10.1016/j.cma.2004.12.017.
53. Zhang, R., Li, L., Zhao, L., Tang, G. (2018). An adaptive remeshing procedure for discontinuous finite element limit analysis. International Journal for Numerical Methods in Engineering, 116(5), 287-307. https://doi.org/10.1002/nme.5925.